

Understanding the full zoo of perovskite solar cell impedance spectra with the standard drift-diffusion model

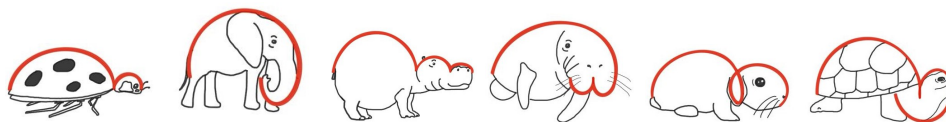
Will Clarke¹, Giles Richardson^{*1}, and Petra Cameron^{*2,3}

¹Mathematical Sciences, University of Southampton, UK

²Institute for Sustainability, University of Bath, UK

³Department of Chemistry, University of Bath, UK

*These authors contributed equally to this work



Abstract

The impedance spectra of perovskite solar cells frequently exhibit multiple features which are typically modelled by complex equivalent circuits. This approach can lead to the inclusion of circuit elements without a sensible physical interpretation and create confusion where different circuits are adopted to describe similar cells. Spectra showing two distinct features have already been well explained by a drift-diffusion model incorporating a single mobile ionic species but spectra with three features have yet to receive the same treatment and have even been dismissed as anomalous. This omission is rectified here by showing that a third (mid-frequency) impedance feature is a natural consequence of the drift-diffusion model in certain scenarios. Our comprehensive framework explains the shapes of all previously published spectra, which are classified into six generic types, each named for an animal resembling the Nyquist plot, and approximate solutions to the drift-diffusion equations are obtained in order to illustrate the specific conditions required for each of these types of spectra to be observed. Importantly, we show that the shape of each Nyquist plot can be linked to specific processes occurring within a cell, allowing useful information to be extracted by a visual examination of the impedance spectra.

1 Background

Perovskite solar cells Since perovskites were first employed in photovoltaic applications as sensitizers in dye-sensitised solar cells [1,2], they have gained enormous interest in the search for cheap and efficient photovoltaics. The template for perovskite solar cells (PSCs) was set by Ball *et al.* [3], with a conventional ‘n-i-p’ thin film architecture, in which the perovskite absorber layer (PAL) is sandwiched between the n-type electron transport layer (ETL) and the p-type hole transport layer (HTL).

The following decade saw a rapid increase in the record power conversion efficiency (PCE) of these devices. At time of writing, this record is 26.1%, matching the current record for monocrystalline silicon solar cells [4], the main commercial technology. Furthermore, the tunable band gap of perovskites makes them an excellent candidate for use in multijunction tandem cells. The current efficiency record for silicon-perovskite tandem cells is 33.7%, surpassing the record for either technology individually and approaching that of the far more expensive GaAs solar cells [4].

Despite the impressive advances in PSCs over the last decade, several challenges still remain in the path to large-scale commercial manufacture. The most pressing of these include long-term stability [5–16] and reliance on toxic materials [17–20]. In order to tackle these challenges, a deeper understanding of the physical processes occurring within the perovskite is required. Standard photovoltaic characterisation techniques are complicated in the case of PSCs by the large densities of slow-moving mobile ion vacancies predicted by atomistic modelling of the perovskite [21]. These mobile ions have been shown to impact device behaviour by modulating the carrier recombination rate [22] and introducing transients on timescales of seconds to hours [23, 24]. Recent work, however, has revealed that the ionic signatures in measured data can provide tell-tale indications of bottlenecks in device efficiency, when analysed using sophisticated modelling [25, 26].

Electrochemical impedance spectroscopy Electrochemical impedance spectroscopy (EIS) is a cheap, easily-conducted and non-destructive technique that is widely used to gather information on recombination losses, ion activation energies and capacitance in PSCs. A small oscillating voltage is used to perturb the cell from a fixed DC voltage (V_{DC}) at a range of frequencies,

$$V = V_{\text{DC}} + V_p \sin(\omega t), \quad (1)$$

where V_p is the voltage amplitude (usually $\approx 10\text{mV}$) and ω is the frequency of the AC voltage component. At each frequency the magnitude (J_p) and phase delay (θ) of the AC current response is recorded and used to construct a complex impedance

$$Z(\omega) = \frac{V_p}{J_p(\omega)} e^{-i\theta(\omega)}. \quad (2)$$

The real and imaginary parts of this impedance are termed the resistance and reactance, respectively. The impedance response of a device is typically visualised in a Nyquist plot, as illustrated in Figure 1, in which a scan in the frequency ω , is represented by a curve in the resistance-reactance plane (with resistance along the x -axis and reactance along the y -axis). Note that throughout this paper we use units of $\Omega \text{ cm}^2$ for simulated impedance due to the planar nature of the model. The information gained from performing impedance spectroscopy is sometimes displayed in the form of a capacitance plot, where the capacitance, $C = \frac{1}{\omega} \text{Im} \left(\frac{1}{Z} \right)$, is plotted against frequency. We note that any conclusions drawn from a Nyquist plot with labelled time constants are therefore naturally extended to the corresponding capacitance plot. Simulated impedance spectra in the main text are displayed as Nyquist plots for easier shape recognition but all corresponding capacitance plots can be found in the SI.

These impedance measurements can reveal much about the internal physics of the device by separating the timescales on which processes occur. Furthermore, they can be performed across a range of DC voltages [27, 28], illumination levels [29, 30], and temperatures [31] to add an extra dimension to the data.

Equivalent circuits A common method of interpreting IS measurements is in terms of equivalent circuits (ECs): hypothetical circuits comprising standard electronic components used to replicate the current-voltage characteristics of a full device [32]. For example, a single semicircle in the Nyquist plot can be replicated by a resistor and capacitor in parallel, which is referred to as an ‘RC circuit’. This circuit has an associated time constant, $\tau = RC$, where R and C are the resistance and capacitance of the resistor and capacitor, respectively. Through parameter-fitting, therefore, a semicircle in a measured Nyquist plot can be ascribed an associated resistance, capacitance, and time constant. Multiple arcs (*e.g.* a low- and high-frequency arc) in Nyquist plots can be reproduced by placing two RC elements in series, *e.g.* [33, 34] or, equivalently, two nested RC circuits, *e.g.* [32]. In addition, such ECs can also be used to reproduce other experimental data, such as current-voltage curves [35].

The fitting of ECs to IS data is computationally cheap and has therefore been widely used as a method of extracting useful information about the internal physics of the cell, but extreme care needs to be taken when ascribing individual circuit elements to physical processes within the cell.

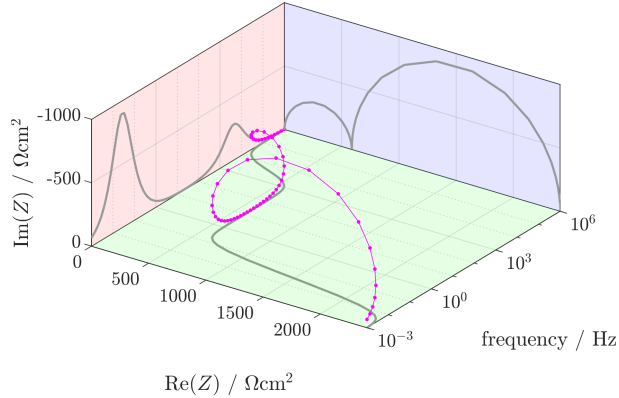


Figure 1: An example impedance spectrum simulated in IonMonger (parameter set A in Table S1) showing the projection onto a Nyquist plot (blue). Projections onto the complex impedance versus frequency plot (red) and the real impedance versus frequency plot (green) are also shown.

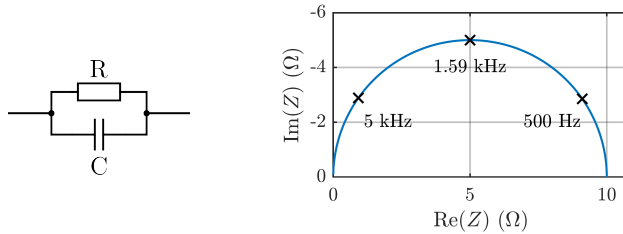


Figure 2: (Left) a basic RC equivalent circuit. (Right) the resulting Nyquist plot when $R = 10 \Omega$ and $C = 10 \mu\text{F}$.

Equivalent circuit fitting is useful where each RC component can be ascribed a well-defined physical origin. This simple correlation between circuit element and physical process breaks down in the impedance response of perovskite solar cells at low frequencies. The **shape** of the low frequency impedance response can be well described by a combination of capacitors, resistors and inductors but the values of the capacitance or inductance extracted **may not be related to any actual physical capacitances or inductances inside the solar cell**. Furthermore, ECs of perovskite solar cells can quickly grow over-complex in the search to more realistically capture the data (see Table 1). In this paper we describe the physical origin of the full family of possible impedance spectra using the standard drift diffusion model. In doing so we avoid the need to invoke ‘giant capacitances’, ‘negative capacitances’ or ‘chemical inductances’ which are too often misunderstood as actual physical capacitances and inductances present in the solar cell [28].

Drift-diffusion models Drift-diffusion (DD) models simulate the internal state of a device by considering the densities of charged species and their response to gradients in electric potential (drift) and number density (diffusion). When applied to PSCs, these models are made significantly more complex by the addition of slow-moving mobile ion vacancies in the perovskite [52], meaning the interpretation used for other photovoltaic technologies can not be directly applied to PSCs [53]. In contrast to ECs, the parameter inputs for drift-diffusion models each have a clear and well-defined physical meaning. These models are, however, computationally expensive to solve numerically [54] and the large number of material input parameters makes data fitting a costly process. Nevertheless, drift-diffusion models have been fitted to IS data from PSCs (see [55–57]).

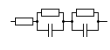
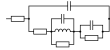
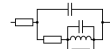
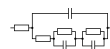
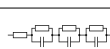
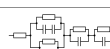

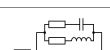




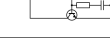
| Circuit | Reference | Circuit | Reference |
|---|-----------|---|-----------|
|  | [36-38] |  | [39] |
|  | [40] |  | [41, 42] |
|  | [43-46] |  | [43] |
|  | [47] |  | [48] |
|  | [49] |  | [50] |
|  | [22] |  | [28] |
|  | [51] | | |

Table 1: Equivalent circuits utilised to model impedance spectra of PSCs.

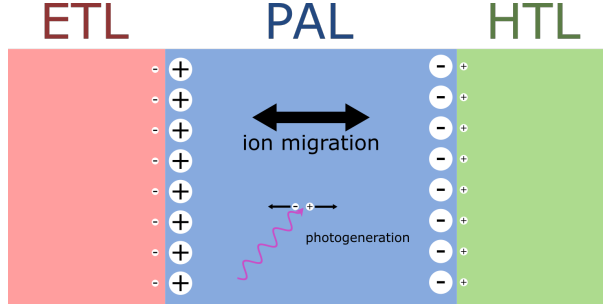


Figure 3: Depiction of the charge distribution in a PSC. Large circles represent ionic charge and small circles electronic charge.

This fitting process has been expedited by utilising a hybrid approach in which initial fitting is performed using a simplified model and results can be tweaked and validated by performing full numerical simulations. Moia *et al.* construct an EC model in order to perform quick parameter-fitting but, crucially, one inspired by the drift-diffusion model and in which each component has a clear physical interpretation. For example, they model material interfaces as transistors coupling ion distribution to electronic injection and recombination [22].

Alternatively, Bennett *et al.* [53] derive approximate analytic solutions to the drift-diffusion model by considering small perturbations to a reduced order model (the surface polarisation model [58, 59]) that has been systematically derived from the underlying drift-diffusion model [58]. In this reduced order model, each layer is divided into a large bulk region and very thin space charge layers (on the order of one Debye length) near material interfaces (see Figure 3). These space charge layers comprise mobile ions in the perovskite and electrons/holes in the ETL/HTL. All three bulk regions are found to be electrically neutral at leading order. Each space charge layer adheres to a nonlinear capacitance relation and the dynamic behaviour of the cell is governed by the slow migration of mobile ion vacancies into/out of the thin Debye layer at one side of the PAL and the depletion region at the opposite side, responding to the applied potential. The advantages of this approach are (i) that the parameter inputs of the simplified model are directly taken from the drift-diffusion model, and (ii) that

the approximate solutions isolate the dominant physical processes and therefore provide insight that is not easily obtained from numerical solutions. However, this approach is based on a set of assumptions regarding the material parameters and is therefore not applicable to all measured data. Specifically, the Bennett approach yields only two semicircles in the Nyquist plot, and is thus not applicable to spectra that show three or more features. The purpose of this work is to extend the insight and understanding provided by Bennett *et al.* [53] to a wider range of PSC designs, and specifically to show that a third impedance feature is a natural consequence of ionic-electronic drift-diffusion in a PSC and not a result of exotic physics. This insight reveals that useful information can be extracted from the shape of the Nyquist plot and the number of features without the need for sophisticated fitting. In Section 2, we identify six categories of Nyquist plot that are commonly obtained from impedance measurements made on PSCs and show that each can be reproduced by a standard drift-diffusion model without the need to invoke exotic physics. In Section 3, we explain the conditions that cause a third impedance feature to appear from the ionic-electronic drift-diffusion model and show how this gives rise to the four archetypical three-feature spectra observed in the experimental literature and examined here in Section 2. This analysis is used in Section 4 to create a framework for diagnosing performance losses in cells which exhibit a third arc in their impedance spectra, alongside discussion of best practices when performing impedance measurements in order to aid meaningful analysis and testing of physical theories. Finally, in Section 5, we draw our conclusions.

2 Classification of spectra found in the literature

The impedance spectrum of a PSC typically exhibits two or more distinct semicircular features, when viewed as a Nyquist plot. Motivated by observed PSC impedance spectra we classify PSC Nyquist plots into one of six categories: two labelled ‘two-feature’ and comprising only two semicircles, and four labelled ‘three-feature’ and comprising three semicircles (as illustrated in Figure 4). For each category of Nyquist plot, we discuss the experimental conditions under which they have been observed and the proposed interpretations found in the literature. We then show that each of these categories of plot can be replicated by a standard ionic-electronic drift-diffusion simulation, without the need to invoke any exotic physics, by providing representative plots obtained using the open-source PSC simulator *IonMonger* [60, 61]. Detailed explanation of how such spectra appear from the standard drift-diffusion model is left until Section 3.

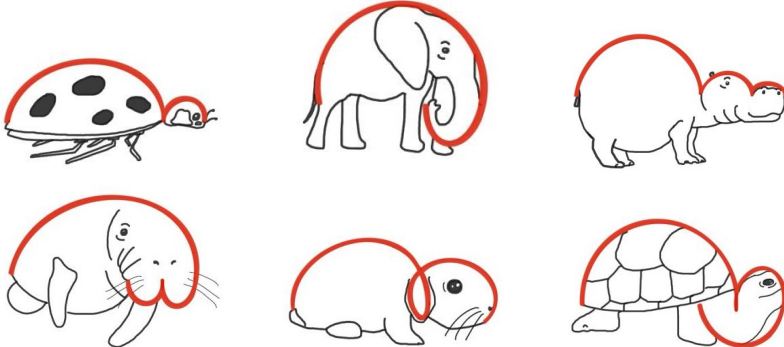
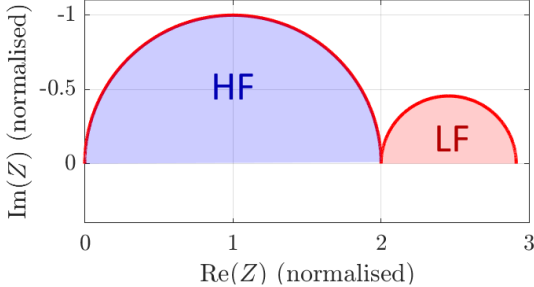
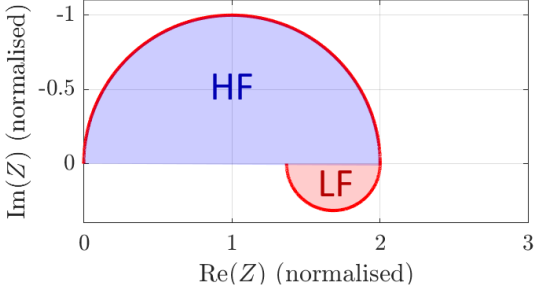


Figure 4: The ‘zoo’ of PSC impedance spectra. From top left to bottom right: the ladybird, the elephant, the hippo, the manatee, the rabbit, and the tortoise.

2.1 Two-feature impedance spectra

We first consider the two-feature Nyquist plots, in which two distinct semicircular features are observed: one at high frequencies (typically on the order of kHz) and one at low frequencies (on the order of mHz-Hz). The high frequency (HF) semicircle is always positive, here meaning lying above the x -axis in the Nyquist plot (*i.e.* $\text{Im}(Z) < 0$). The low frequency (LF) feature, however, can appear as either positive [27, 29, 51, 62] or negative [51, 63, 64], as depicted in Figure 5, and this difference leads us to subdivide such Nyquist plots into two classes: the ladybird () and the elephant (), named for the animals they resemble.

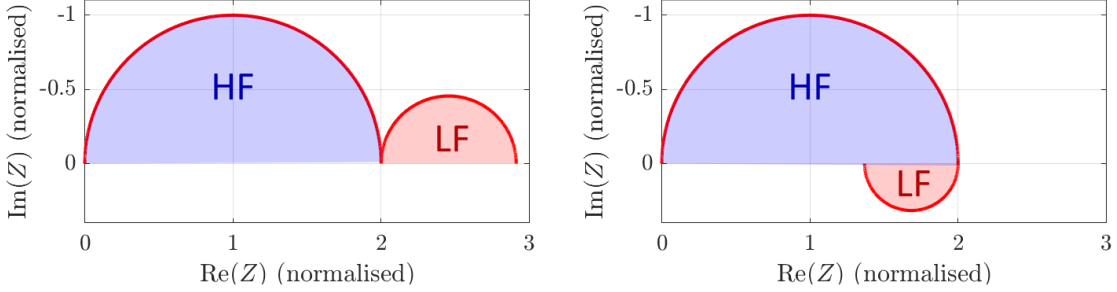


Figure 5: Two-feature Nyquist plots: the ladybird (left) and the elephant (right). The impedance has been normalised such that the radius of the HF arc is 1. These plots were generated using the analytic model of impedance presented by Bennett *et al.* [53].

In the following, we discuss the origin of the HF feature, scenarios in which positive and negative LF features have been observed experimentally, and review the various explanations put forward in the literature and the corresponding modelling.

2.1.1 The high-frequency arc

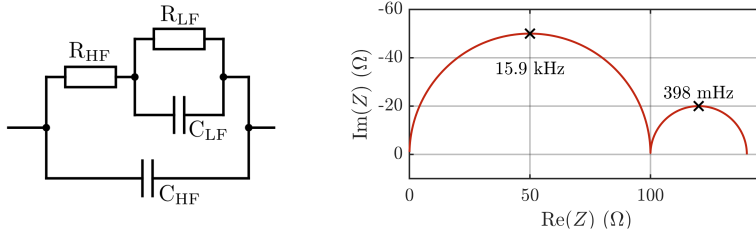


Figure 6: The "RC-RC" equivalent circuit (left) often used to model two-feature PSC impedance spectra and (right) the corresponding Nyquist plot for $R_{\text{LF}} = 40 \Omega$, $R_{\text{HF}} = 100 \Omega$, $C_{\text{LF}} = 10 \text{ mF}$, and $C_{\text{HF}} = 100 \text{ nF}$.

Impedance spectra showing two distinct semicircles are commonly modelled by an 'RC-RC' equivalent circuit, comprising two nested RC circuits, corresponding to the high and low frequency arcs, respectively. This EC is shown in Figure 6, along with the resulting Nyquist plot.

The high frequency capacitance was found by Pockett *et al.* [62, 65] to be consistent with a geometric capacitance,

$$C_{\text{HF}} = \frac{\varepsilon A}{d}, \quad (3)$$

due to being independent of applied bias and illumination intensity. This was subsequently confirmed by Guerrero *et al.* via measurements of the dependence of HF capacitance on the width of the perovskite layer [39] and by Bennett *et al.* from theoretical consideration of the drift-diffusion model [53]. The

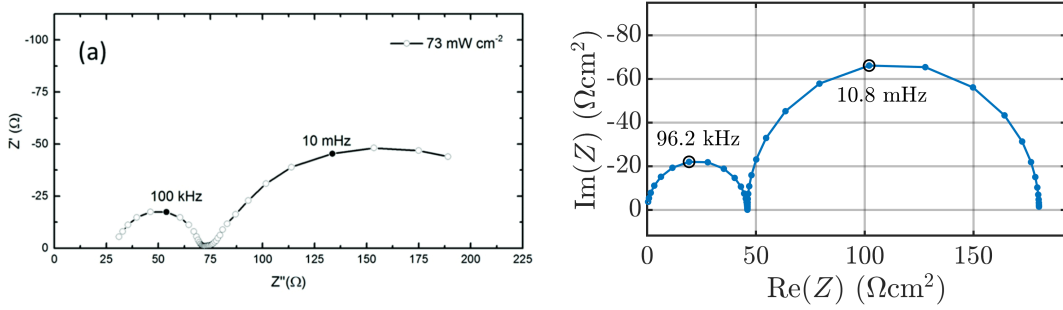




Figure 7: Examples of two-feature impedance spectra of perovskite solar cells exhibiting the ladybird shape. Left panel is reproduced from [65] (under CC BY 3.0) and was measured from a $\text{TiO}_2/\text{MAPbI}_{3-x}\text{Cl}_x/\text{Spiro}$ cell under 73 mW cm^{-2} illumination and at $V_{\text{DC}} = V_{\text{OC}}$. Right panel is obtained from simulation of the drift-diffusion model (S1-S17) performed in IonMonger between 1 mHz and 1 MHz, under 1 Sun illumination and at $V_{\text{DC}} = 0.70\text{V}$. Material parameter values for the simulated spectrum can be found under ‘Cell A’, in Table S1. Note that Z' and Z'' are used to denote $\text{Re}(Z)$ and $\text{Im}(Z)$, respectively.

parallel resistance at high frequencies is usually attributed to a recombination resistance [53,55,62]. It has been suggested that R_{HF} contains a transport resistance [32,66] but this usually only amounts to a small distortion under carefully pre-selected conditions. This shows the drawbacks of using equivalent circuits to model impedance data, namely that the meaning of the components is ambiguous and that, in an attempt to more realistically capture the data, circuits can quickly become over-complex.

The HF semicircle also always appears in the ionic-electronic drift-diffusion model (see Figures 7b, 8b, 11b, 12b, 13b, 14b). While the origin can be difficult to uncover from numerical simulations alone, due to the complexity of the model, an analytic model of impedance was recently derived systematically from the drift-diffusion equations by Bennett *et al.* [53]. This approach avoids the pitfalls of ECs since it is derived from well-established physics, and its simplicity also gives better physical intuition, and much reduced computational cost, when compared to direct numerical DD simulations. It is concluded that the HF resistance in the DD model is consistent with a recombination resistance, and the HF capacitance is purely a geometric capacitance, caused by the out-of-phase contribution of the displacement current to the total current due to polarisation of the perovskite layer. In this work however, we show that there are circumstances in which the DD model predicts a high frequency capacitance not solely resulting from the geometric capacitance. This is detailed in Section 3.3.5.

2.1.2 Positive LF feature: the ladybird

Spectra with a positive LF feature (the ladybird ) are frequently observed in PSCs (see, *e.g.* [27, 29, 62, 67, 68]). This feature has been observed at DC voltages ranging from short-circuit [69–71] to open-circuit [51, 62, 72] and at illumination intensities from darkness [29, 73, 74] to 1 Sun equivalent [29, 51, 67]. An example of an experimental Nyquist plot, taken from [65], that displays this feature is shown in Figure 7a. Here the LF arc is significantly larger than the HF arc, corresponding to HF resistance that is larger than the LF resistance (in the RC-RC equivalent circuit). However, this condition does not always hold (see, for example, [75]). While these two-feature spectra are well-replicated by the RC-RC circuit, the origin of the LF resistance and apparent capacitance has been widely debated. Proposed explanations in the literature include the impedance of trap states [76], carrier accumulation near interfaces [39, 77], a ‘giant dielectric effect’ [27, 78], and ionic diffusion [79, 80].

An example of a ladybird impedance spectrum , obtained through drift-diffusion simulations, is shown in Figure 7b. Numerical simulations of the ionic-electronic drift-diffusion model suggest that the LF feature is associated with the migration of mobile ion vacancies [56]. The apparent LF capacitance is therefore interpreted as ionic modulation of the recombination rate due to the

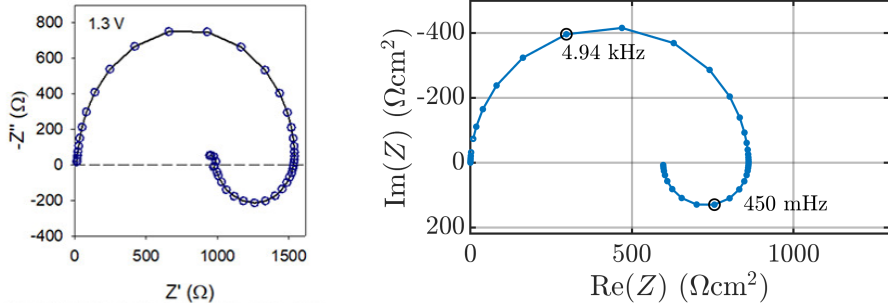


Figure 8: Examples of two-feature impedance spectra of perovskite solar cells showing a positive low frequency feature (the elephant). Left panel is reproduced from [35] (under CC BY-NC-ND 4.0) and was measured from a $\text{TiO}_2/\text{MAPbBr}_3/\text{Spiro}$ cell in the dark and at $V_{\text{DC}} = 1.3$ V. Right panel is obtained from simulation of the drift-diffusion model (S1-S17) performed in IonMonger between 10 mHz and 10 MHz, under 1 Sun illumination and at $V_{\text{DC}} = 0.89$ V. Material parameter values for the simulated spectrum can be found under ‘Cell B’, in Table S1. Note that Z' and Z'' are used to denote $\text{Re}(Z)$ and $\text{Im}(Z)$, respectively, contrary to Figure 7.

polarisation of the ionic charge in the perovskite layer, but the source of the LF resistance is less clear. Proposed explanations include a transport resistance of the ions themselves and a recombination resistance modulated by the ionic distribution [22].

Once again, the approximate solutions to the drift-diffusion equations obtained by Bennett *et al.* clarify the underlying mechanism [53]. At low frequencies, the migrating ions can only partially screen the electric field in the perovskite bulk, and the flow of ionic charge across the layer lags behind the oscillating voltage. The lagging space charge layers then modulate the recombination current, creating an impedance response at frequencies associated with ion migration in the perovskite layer, *i.e.* the flux of vacancies entering/leaving the thin charge layers at the edges of the perovskite (see Figure 3). The LF capacitance is therefore dependent on the properties of the mobile ions and the associated resistance depends on the dominant source of recombination. It is important to note that the LF capacitance is an apparent capacitance and not a true physical capacitance [22, 57, 65]. Bennett *et al.* determine that no LF arc appears when the dominant energy loss is bimolecular bulk recombination in the perovskite, but may appear where the dominant energy loss is Shockley-Read-Hall (SRH) recombination in either the bulk or on the perovskite interfaces. For this reason, bimolecular recombination is neglected in the simulations presented here since it is a requirement that SRH is the dominant form of recombination where two or more impedance features are present. Notably, reintroducing a small amount of bi-molecular recombination changes the observed resistances of the spectrum but not its qualitative shape or time constant. Simulated spectra with the inclusion of bi-molecular recombination can be found in the supplementary information. Furthermore, analytic expressions are derived in [53] for the LF resistance and capacitance in terms of the material parameters used as input for the DD model.

2.1.3 Negative LF feature: the elephant

The LF impedance feature may also appear below the x -axis, corresponding to the imaginary part of the impedance being positive, and denoted here as ‘the elephant’ (see Figure 4). An example of such a spectrum, taken from experiment, is shown in Figure 8a. This has been modelled in the literature by an RC-RC equivalent circuit with negative low-frequency resistance and capacitance [33, 34], *i.e.* $R_{\text{LF}}, C_{\text{LF}} < 0$. Once again, this highlights the non-physical nature of EC models, and the difficulty in interpreting them in terms of real cell properties. The negative LF apparent capacitance has also been modelled by the addition of a ‘chemical inductor’ to the EC [28], the physical origin of which has been linked to ion-controlled surface recombination [81]. As outlined earlier, the values of the inductance extracted from equivalent circuit fitting does not relate directly to any physical inductance within the

solar cell.

However, as shown in Figure 8b, the drift-diffusion model can replicate the apparent negative LF capacitance without recourse to exotic or unexplained physics. The parameter set that gives rise to an impedance response with apparent negative capacitance in Figure 8b (*i.e.* Cell B in Table S1) differs from the set used to generate a response with positive capacitance in Figure 7b (Cell A in Table S1) by only a few parameters. The most significant difference between the two parameter sets is in the recombination rate; in particular, the bulk SRH recombination in Cell A is electron-limited whilst that in Cell B is hole-limited. As explained by Bennett *et al.* [53], the switching between electron-limited and hole-limited bulk recombination causes a change in the sign of the LF feature when the cell is otherwise unchanged. Furthermore, Bennett and coworkers show that negative LF features result only from bulk SRH recombination and not from recombination on the perovskite interfaces.

We emphasise again that the LF feature is not a consequence of a true capacitance, *i.e.* a current flow resulting from a dipolar charge accumulation. While the thin space charge layers in which ionic vacancies build up or deplete do indeed charge and discharge on these timescales, the current associated with accumulation and depletion of vacancies in these layers is negligible. Instead, the variations in the measured current result from a modulation of electronic current caused by changes to the ionic distribution. The apparent capacitance is thus a consequence of ionic modulation of the recombination rates [22, 65].

2.2 Three-feature impedance spectra

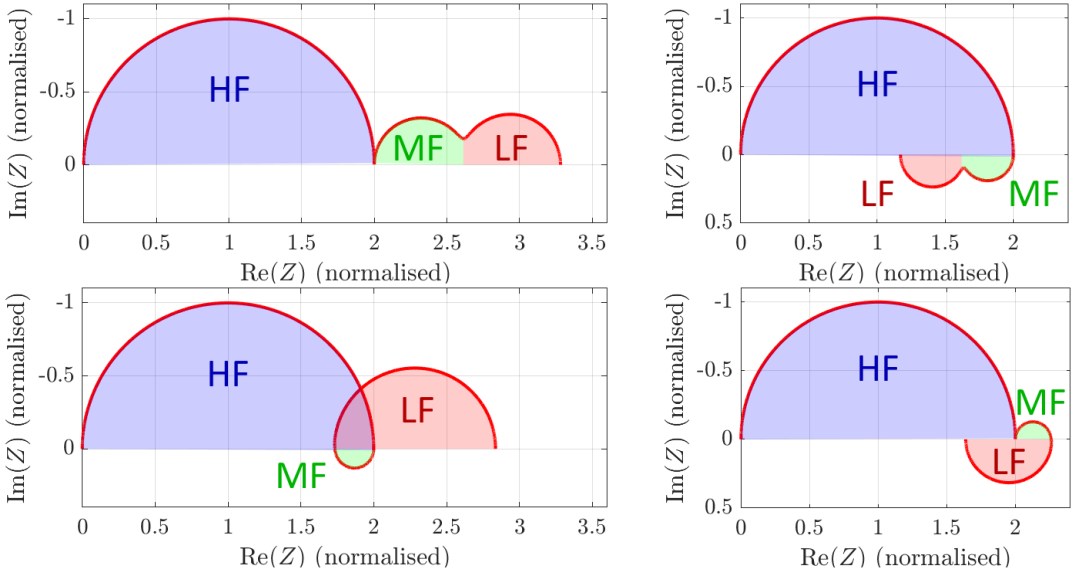




Figure 9: The four classifications of spectra exhibiting a third mid-frequency feature. (Top left) hippo, (top right) manatee, (bottom left) rabbit, and (bottom right) tortoise. These plots were generated using the analytic model of impedance based on the modified surface polarisation model (17).

Whilst many PSCs exhibit the two-feature EIS spectra (ladybird  and elephant ) which are well-explained by the analytic model developed in [53], there are many reported instances of PSCs exhibiting EIS spectra with three features. Here we review the literature associated with three-feature spectra and classify such spectra into four categories, based on the features observed in their Nyquist plots (as illustrated in Figures 4 and 9). In all four cases, we observe the presence of a third mid-frequency (MF) semicircular feature that links the standard LF and HF arcs. Furthermore, we demonstrate that each of these four types of three-feature spectra can be replicated by standard drift-

diffusion simulations, without recourse to additional physics, and are well reproduced by our reduced order model (17), detailed in Section 3. As illustrated in Figure 10, the three-feature spectra computed from standard drift-diffusion simulations divide into four archetypes, depending on whether the mid- and low-frequency arcs appear above or below the axis in the Nyquist plot. In Section 3 the processes that give rise to these MF features are explained with reference to the standard PSC drift-diffusion model.

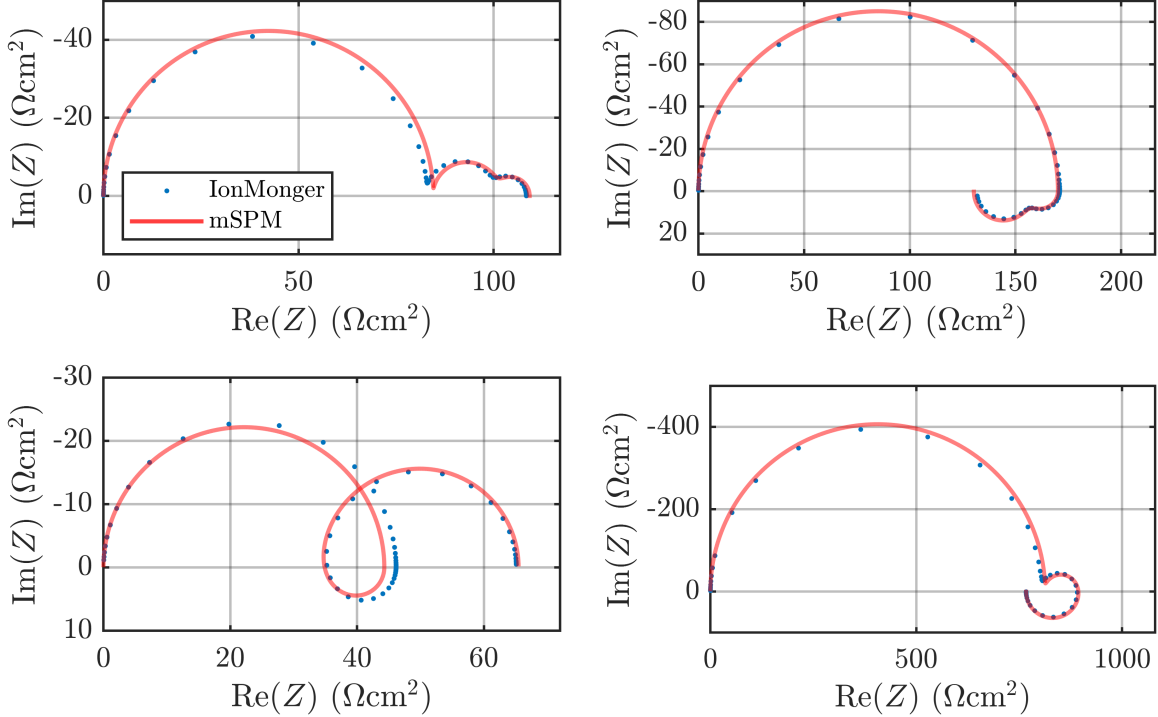
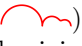


Figure 10: The four three-feature impedance spectra shown in Figure 9, replicated in both numerical solutions of the full drift-diffusion model (S1-S17) using IonMonger (blue circles) and the reduced order model (17) detailed in Section 3 (red lines). For details of the simulation parameters, see Figures 11-14, in which these simulations are reproduced and compared with experimentally measured spectra.

2.2.1 Positive MF and LF features: the hippo

The most straightforward and easily recognisable of the three-feature PSC spectra is the hippo, as depicted in Figure 9a, in which a third, positive, MF semicircle joins the positive LF and HF features (corresponding examples of experimentally observed and simulated Nyquist plots are shown in Figure 11). As shown in Figure 11a, there is often an overlap between the LF and MF semicircles, meaning it can be difficult to distinguish between two-feature and three-feature spectra. Hippo spectra are almost always reported for large DC voltages, in the neighbourhood of (or above) the maximum power point (MPP) and under illumination [31, 43, 65, 82–84]. An exception to this was reported by Aeineh *et al.* using a DC voltage of 0.2V [42] but there the MF feature was far smaller than either the HF or LF features, suggesting that the MF feature becomes more prominent at large voltages. There appears to be no correlation with architecture or material choice.

While hippo spectra () have been widely observed [31, 42–44, 65, 82–84], no consensus has been reached on their physical origin. Numerous equivalent circuits have been utilised to model the extra feature [32, 85] but a physical interpretation of the additional circuit elements is rarely offered. Over three separate studies, Cameron and coworkers studied the appearance of hippo spectra at different

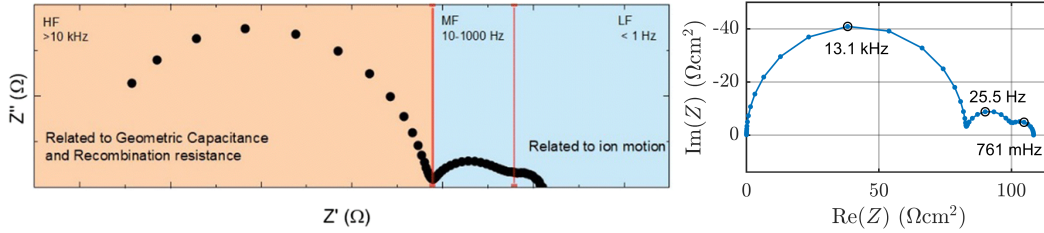






Figure 11: Examples of three-feature impedance spectra of perovskite solar cells showing positive LF and MF features (the hippo shape). Left panel is reproduced from [31] (under CC BY 3.0) and was measured from a NiO/MAPbI₃/PCBM cell under illumination and at $V_{DC} = V_{OC}$. Right panel is obtained from simulation of the drift-diffusion model (S1-S17) performed in IonMonger between 1 mHz and 10 MHz, under 1 Sun illumination and at $V_{DC} = 1$ V. Material parameter values for the simulated spectrum can be found under ‘Cell C’, in Table S1.

temperatures and for different perovskite compositions [31,65,82]. They concluded that the MF feature was due to a thermally-activated process and was consistent with the migration of iodide vacancies throughout the crystal, despite occurring on timescales roughly three orders of magnitude faster than the iodide-induced LF feature.

Despite the suggestion of exotic ECs, it is possible to obtain hippo Nyquist plots from numerical simulations of the standard mixed ionic-electronic PSC drift-diffusion model. One such spectrum, which is computed using IonMonger from the Cell C parameter set in Table S1, is shown in Figure 11b. In this case both the MF (approx. 6 Hz) and LF (approx. 150 mHz) features are smaller than the HF one (approx. 130 kHz) but a wide range of variations on this shape can be obtained by altering material parameters. The key differences between this parameter set and those used to obtain standard, two-feature spectra (Cells A  and B ) are (i) an increase in the perovskite valence band maximum from -5.4 eV to -5.3 eV and (ii) a swapping of the ETL and HTL permittivities to reflect the use of an organic ETL and inorganic HTL in Figure 11a. The decreased band offset between the perovskite and the HTL causes an increase of hole leakage from the transport layer back into the perovskite, increasing the typical hole densities in this region. At room temperature, a change in band edge energy of 0.1 eV corresponds to an increase in carrier density by a factor of roughly 50. The change in transport layer permittivities, however, alters the steady state ionic distribution in the perovskite layer [59]. The process by which these parameter changes induce an additional impedance feature is explained in detail in Section 3. It is worth noting that there is some overlap between impedance features in both experiment and simulation [86]. In fact, simulations show the two features are only well-distinguished in a relatively narrow region of the DC voltage. In this work we restrict our analysis to this region, in which they are distinct, but future work will address the evolution and merging of the two features across a broader range of voltages.

2.2.2 Negative MF and LF features: the manatee

The negative analogue of the hippo () is the manatee (), depicted in Figure 9b (experimental observation and simulation shown in Figure 12), in which both the MF and LF arcs lie below the axis. To the authors’ knowledge there are only three reports of such spectra in the literature, all occurring at DC voltages of at least 0.5V and for illumination intensities ranging from 0.05 to 1 Sun equivalent [28,33,40]. Naturally, no conclusions can be drawn about the correlation between architecture and material choices with the appearance of this feature from such a small sample size.

An impedance spectrum obtained from a triple-cation PSC in [33] appears to have two negative features that overlap very closely, meaning a separate MF feature was not identified and therefore no explanation was made of possible origins. Similarly, a spectrum was measured by Hernández-Balaguera and Bisquert [28] that appears to show the beginning of a second negative feature but the

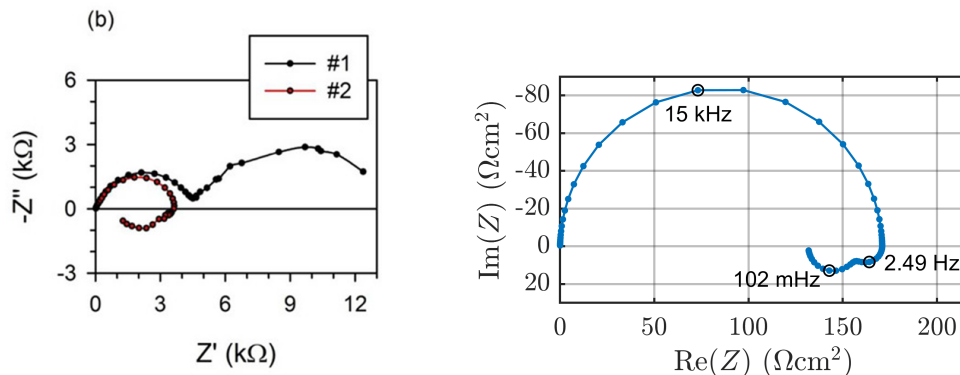


Figure 12: Examples of the manatee Nyquist shape, showing negative LF and MF features. Left panel is reprinted (adapted) with permission from [40] (Copyright 2017 American Chemical Society) and was measured from a $\text{TiO}_2/\text{CsPbBr}_3/\text{PTAA}$ cell under 1 Sun illumination and at $V_{\text{DC}} = 0.7$ V. Right panel is obtained from simulation of the drift-diffusion model (S1-S17) performed in IonMonger between 10 mHz and 5 MHz, under 0.5 Sun illumination and at $V_{\text{DC}} = 0.87$ V. Material parameter values for the simulated spectrum can be found under ‘Cell D’, in Table S1.

lack of measurements below 1 Hz prohibits resolution of this possible feature. Given the frequency range of the experiment, we posit that the feature identified by the authors as a LF response is in fact a MF response and the Nyquist plot shows only the beginning of a third, true LF feature. Apparent negative capacitance at mid-frequencies was also reported by Fabregat-Santiago *et al.* [40], who modelled the effect using an inductor in an equivalent circuit. Notably, however, a different EC was adopted depending on whether ‘negative capacitance’ was observed, precluding the model from providing a unified theory of the devices. The inductor fits the observed response, but once again its physical origin is less clear.

The Nyquist plot showing a manatee (🐬) shape taken from the literature in Figure 12a is replicated using numerical simulations of the standard ionic-electronic PSC drift-diffusion model in Figure 12b. A small MF arc appears at approximately 2.5 Hz, followed by a slightly larger LF arc at approximately 100 mHz. This simulation is consistent with our explanation of the spectrum reported by Hernández-Balaguera and Bisquert [28], as a cutoff at 1 Hz would show the entire MF feature but almost none of the LF feature. The parameter set used to generate this Nyquist plot (Cell D in Table S1) is similar to Cell C (hippo 🐘) apart from two key changes: (i) the transport layer permittivities have been swapped to be consistent with an inorganic ETL and an organic HTL, and (ii) the SRH recombination pseudo-lifetimes have been swapped, changing the bulk SRH recombination from electron-limited to hole-limited.

2.2.3 Negative MF and positive LF features: the rabbit

The rabbit Nyquist shape (🐰), as illustrated in Figure 4, is one of the most commonly observed three-feature spectra. Created by the joining of a positive LF arc to a negative MF arc, they are easily identified by a small region of the Nyquist plot being completely enclosed by the curve. If the MF arc is large and the LF arc small, however, the loop may no longer close and the Nyquist plot takes the form of a spiral (🌀). No distinction between the two is made here. Once again this exotic feature is usually observed for large DC voltages and under illumination [45, 46, 48, 82, 87, 88]. Experiments conducted by Wang *et al.* show that loops in the EIS spectra become larger as the DC voltage is increased and are also affected by ETL material choice [47].

The so-called ‘inductive loop’ was modelled by Muscarella *et al.* via the addition of a third resistor-capacitor element to the RC-RC circuit with the LF and MF RC elements attributed to ‘slow electrochemical’ processes in the cell [46]. We note, however, that the resistance and capacitance of the

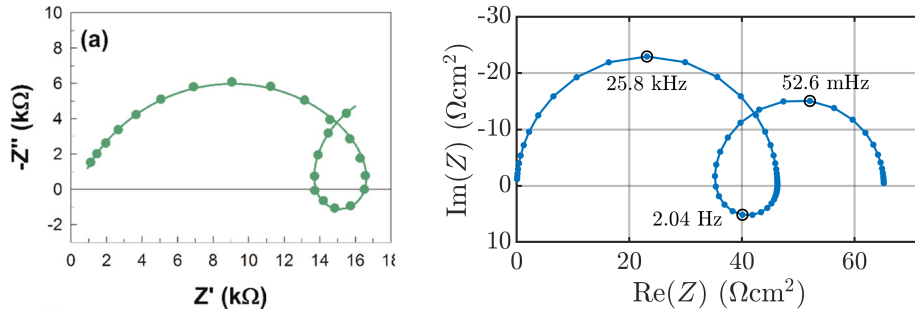


Figure 13: Examples of three-feature impedance spectra of perovskite solar cells showing the rabbit Nyquist shape, *i.e.* a negative MF arc and a positive LF arc. Left panel is reprinted (adapted) with permission from [48] (Copyright 2017 American Chemical Society) and was measured from a cell under illumination and at $V_{DC} = 0.7$ V. Right panel is obtained from simulation of the drift-diffusion model (S1-S17) performed in IonMonger between 1 mHz and 1 MHz, under 1 Sun illumination and at $V_{DC} = 1.0$ V. Material parameter values for the simulated spectrum can be found under ‘Cell E’, in Table S1.

added RC components were both negative, and cannot therefore be linked to a true resistance and capacitance. More studies have modelled the loop by adding an inductor in parallel with the third (MF) R-C element [39,47,48,50]. Once again, however, the physical origins of this inductance are not clear.

The Nyquist plot showing a loop feature taken from the literature in Figure 13a is replicated using numerical drift-diffusion simulations in Figure 13. The negative MF arc (2.04 Hz) bridges the HF arc (25.8 kHz) and the LF arc (52.6 mHz). Whereas Cells C (🐇) and D (🐇) feature a reduced perovskite-HTL valence band offset, Cell E (🐇) instead features a reduced perovskite-ETL conduction band offset. The effect is to increase the typical densities of electrons in the perovskite layer by a factor of approximately 200. Similarly, the HTL has a lower effective doping density, resulting in fewer holes leaking into the perovskite. Energy loss occurs via electron-limited SRH recombination in the perovskite bulk, as in Cell A (🐇) and Cell C (🐇).

2.2.4 Positive MF and negative LF features: the tortoise

The final class of three-feature spectra is the tortoise (🐢), in which a positive MF feature joins a negative LF feature to the standard (positive) HF feature, as illustrated in Figures 4 and 9d. Examples of an experimental and computationally generated plot of this kind are shown in Figures 14a and 14b, respectively. The LF arc can be larger than the MF, reaching underneath the HF arc [32], or smaller than the MF [89]. Once again this type of spectrum has only been reported for large DC voltages [37,38,66] and never near short-circuit. Illumination intensities under which inverted spirals have been observed range from total darkness [89] to 1 Sun equivalent [32].

The intermediate feature has been modelled by an additional R-C element in the equivalent circuit model but once again without a valid explanation of its physical origin [32]. In pursuit of modelling these three-feature spectra, ECs can quickly grow to exceed 10 electronic components [66], meaning both physical interpretation and parameter fitting become much more difficult than for the simple RC-RC circuit, used to model a spectrum with only two arcs.

The (experimental) tortoise Nyquist plot shown in Figure 14a is replicated in Figure 14b with a simulation of the standard ionic-electronic PSC drift-diffusion model using the parameter set for Cell F in Table S1. The positive MF peak appears at approximately 6 Hz, and the negative LF peak at approximately 220 mHz. Cell F (🐢) has a smaller perovskite-ETL conduction band offset than Cells A (🐇) and B (🐇), which both produced two-feature impedance spectra.

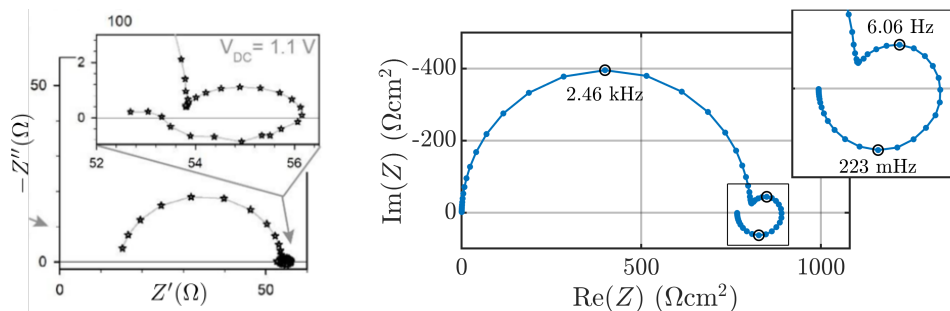


Figure 14: Examples of three-feature impedance spectra of perovskite solar cells showing the tortoise Nyquist shape, *i.e.* a positive MF arc and a negative LF arc. Left panel is reprinted (adapted) with permission from [32] (Copyright 2017 American Chemical Society) and was measured from a $\text{TiO}_2/\text{MAPbI}_3/\text{Spiro}$ cell under 1 Sun illumination and at $V_{\text{DC}} = 1.1$ V. Right panel is obtained from simulation of the drift-diffusion model (S1-S17) performed in IonMonger between 1 mHz and 1 MHz, in the dark and at $V_{\text{DC}} = 1.1$ V. Material parameter values for the simulated spectrum can be found under ‘Cell F’, in Table S1.

2.2.5 Summary

The four classes of three-feature impedance spectra observed in PSCs have all been reproduced using complex equivalent circuit models that do little to reveal their physical origins. However, as shown here, all four classes of spectra can be reproduced using the standard, well-validated [52, 56, 59, 90] ionic-electronic PSC drift-diffusion model, given appropriate parameter sets. Crucially, this drift-diffusion model is based on well-understood physics and so allows us to draw conclusions about the physical origins of these spectra. In particular, it is observed that the parameter sets used to generate three-feature impedance spectra all use physically reasonable values and only differ from those that give rise to two-feature spectra in one key aspect: one of the perovskite-transport layer band offsets is reduced, allowing charge carriers to leak into the perovskite from the transport layer at relatively high densities. It is worth remarking that which particular three-feature spectrum is observed depends on the limiting recombination type (*i.e.* whether it is electron-limited or hole-limited). Notably, one of the key assumptions made in deriving the analytic impedance model presented by Bennett *et al.* [53] is that carrier densities in the perovskite are small enough that they do not significantly influence the electric potential. The link between three-feature spectra and high leakage of carriers into the perovskite therefore explains why Bennett’s analytic impedance model is not applicable to the parameter sets used here to generate three-feature impedance spectra.

3 Predictions of the drift-diffusion model

Having identified the link between a reduced transport layer band offset and the impedance spectra with three arcs, it is important to explain how these solutions arise from the standard PSC drift-diffusion model. In scenarios where the impedance spectra consist of only two arcs, Bennett *et al.* [53] were able to obtain analytic expressions which relate the low- and high-frequency resistances and capacitances to parameters in the drift-diffusion model by looking for the linear response of a reduced order model (termed the **Surface Polarisation Model**, or SPM) to a small oscillating voltage. The SPM has in turn been derived, in a certain asymptotic limit [58, 59], from the standard drift-diffusion model. In particular, it is assumed that the Debye lengths of the carriers are much greater than the width of the perovskite layer b , so that carriers are unable to screen the electric field from the perovskite layer. In the regimes in which three-feature impedance spectra are observed, at least one of the carrier densities is sufficiently high to at least partially screen the field from the perovskite

layer. This explains why the analysis of Bennett *et al.* is incapable of predicting three-feature spectra. We have already extended their results, in Section 2, by showing that spectra with a third, mid-frequency, feature can be reproduced by the standard ionic-electronic PSC drift-diffusion model, with an appropriate parameter set in which one of the perovskite-transport layer band offsets is reduced sufficiently to produce a relatively high density of one of the charge carriers in the perovskite. This leads us to conclude that the physics required to reproduce three-feature spectra is already present in the standard PSC drift-diffusion model, even if it is absent in the scenarios considered in [53]. In order to generalise the results of [53] to scenarios in which three Nyquist features are observed it is first necessary to derive a reduced order model from the standard drift-diffusion model in the appropriate parameter regime. This model was recently derived in order to investigate the phenomenon known as inverted hysteresis in PSCs [25], where it is termed the **modified Surface Polarisation Model**, or mSPM. The impedance solutions to the SPM of a PSC that have been derived by Bennett *et al.* [53] can thus be re-derived with appropriate changes to the assumptions in order to capture this region of the parameter space.

3.1 The standard PSC drift-diffusion model

Our analysis is based on the standard PSC drift-diffusion model, which considers the transport and electrostatic interactions of both ion vacancies and electronic charge carriers. This model is reformulated in the supplementary information (S1-S17). and it, or minor variations of it, have been shown to accurately approximate the behaviour of real devices across a wide range of conditions, and for a variety of characterisation techniques [52, 55, 56, 58–60, 91–94].

The model is based on a common PSC architecture, in which the PAL is sandwiched between the ETL and the HTL, which are, in turn, abutted by metal contacts. In addition to the standard conduction band electrons and valence band holes, conduction in the PAL occurs via migration of positively charged ion vacancies [21]. It is assumed that these vacancies are balanced by an immobile background density of negative ion vacancies such that the net ionic charge across the entire PAL is zero. While some studies have suggested that a second (negative) mobile ion species is present in the perovskite, Bertoluzzi *et al.* conclude that this can only be the case if the diffusion coefficient is even smaller than that of the anion vacancies [95]. The second ionic species is therefore assumed to be immobile in the present study under the assumption that its motion would not be visible on the timescales considered. It is further assumed that the transport layers are sufficiently highly doped that the minority carrier densities in these layers are negligible, as are the effects of charge recombination. The full charge transport model results in a complex system of partial differential equations coupled across the three layers, which exhibit severe numerical stiffness due to the disparity in timescales between electronic and ionic motion and the small Debye length of the mobile ion vacancies [54, 58]. As a result, obtaining accurate solutions is challenging.

Many groups opt for a suitably tailored numerical approach to solving the model, which is capable of overcoming the stiffness of the problem [56, 60, 61, 90, 92]. However, the complexity of the model means that the results produced by such an approach offer limited physical insight. In particular, underlying trends are difficult to recognise and it is hard to attribute a behaviour to a single dominant physical mechanism.

3.2 The surface polarisation model: a reduced order model of charge transport in a PSC

An alternative approach to solving the standard PSC drift-diffusion model is by using an asymptotic method (based on matched expansions) to approximate the DD model by a much simpler, and more tractable, reduced order model (see [52, 58, 59]). This model consists of a single nonlinear ordinary differential equation (in time) for the surface charge density $Q(t)$ stored in the space charge layers at the perovskite/transport layer interfaces and, once $Q(t)$ has been computed, allows the electric

potential distribution across the cell, $\phi(x, t)$, to be uniquely determined. The derivation of the SPM is based on four key assumptions:

- (i) the Debye lengths of mobile vacancies in the PAL, and of the majority carriers in the transport layers, are much smaller than the layer thicknesses;
- (ii) the electron and hole Debye lengths in the PAL are much larger than the PAL thickness;
- (iii) the electronic carriers move much faster than ion vacancies across all three layers; and
- (iv) the carriers in the transport layers are highly mobile.

In the appropriate parameter regime the potential $\phi(x, t)$ determined by the SPM has been shown to be a very good approximation to that determined by the standard PSC drift-diffusion model [53,58,59]. In this work we assume a mobile ion density ($\approx 10^{19} \text{ cm}^{-3}$) that is arguably at the higher end of the range commonly attributed to this parameter, but is in line with the atomistic modelling undertaken in [96]. We note, however, that the Nyquist shapes reproduced by our simulation can also be obtained with lower values of the mobile ion density, as calculated by some groups [97] and that assuming lower mobile ion density thus does not qualitatively change our conclusions.

Furthermore, the algebraic expressions for the ideality factor (n_{el}) and the low and high frequency apparent capacitances and resistances (C_{LF} , R_{LF} , C_{HF} and R_{HF}), measured in an impedance spectroscopy experiment, that are given in [53] are derived directly from the (approximate) SPM. Nevertheless, in the appropriate parameter regime, they agree very closely with the values of these quantities computed directly from simulations of the much more complex PSC drift-diffusion model.

3.3 The modified surface polarisation model

Whilst the SPM performs very well as an approximation to the standard PSC drift-diffusion model over a wide range of realistic parameter values, a theoretical investigation of inverted hysteresis by Clarke *et al.* [25] has shown that some real devices are not well-described by the SPM, even though simulations based on the standard PSC drift-diffusion model still accurately capture their behaviour. In turn, this implies that for these devices, at least one of the asymptotic assumptions used to derive the SPM is invalid. In this instance it is shown that relatively high electronic carrier densities in the PAL invalidate assumption (v), leading to a carrier Debye length comparable to (or shorter than) b , the PAL width, and resulting in partial screening of the electric field from the interior of the PAL. In order to account for such scenarios, Clarke *et al.* [25] derive a modification to the surface polarisation model, termed the **modified surface polarisation model** (mSPM), which accounts for the partial screening by charge carriers and which is restated in the Appendix (12-15). This model pertains to scenarios in which the band offsets between the PAL and the highly-doped transport layers are small enough to allow significant leakage of carriers into the perovskite from the adjacent transport layers. These are exactly the same conditions for which simulations of the standard PSC drift-diffusion model display three-feature impedance spectra (as described in Section 2). Following the same approach as Bennett *et al.* [53], this reduced order model can be linearised in terms of a small voltage perturbation to obtain an analytic solution for impedance (Eq. 17; for derivation, see ESI). In Figure 10, the analytic solution for impedance from the mSPM is validated against numerical solutions to the full PSC drift-diffusion model for an example of each of the four classes of three-feature impedance spectra discussed in Section 2.

In [25] it is shown that the mSPM extends the accuracy of the SPM to parameter sets which give rise to inverted hysteresis. As shown in Figure 15, the principle change in moving from the SPM to the mSPM is that the electric field in the PAL bulk is no longer spatially uniform, because it is now partially screened by large densities of charge carriers. Here the evolution of the electric potential in the PAL is still determined by the flow of slow-moving ions into (and out of) the space-charge layers at transport layer interfaces, which is driven by the electric fields local to the interfaces. However, the field is instantaneously, and at least partially, screened by the presence of large numbers of electronic

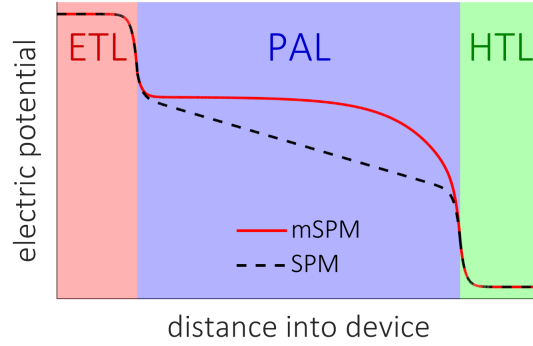


Figure 15: Illustration of electric potential in the modified surface polarisation model (mSPM) and the standard surface polarisation model (SPM). The electric potential is always linear in the PAL bulk under the SPM but this restriction does not apply to the mSPM.

carriers, which in turn affects the flow of ions into (and out of) the space-charge layers. The derivation of an impedance model using leading order solutions under a sinusoidal voltage perturbation is included in the supplementary information but the qualitative behaviour of solutions to the model and some useful results are described in the following sections. We note that the standard SPM is a special case of the mSPM, which means that the impedance model that we derive from the mSPM is still valid for any spectrum for which the SPM is appropriate.

3.3.1 Timescales of ionic motion

Despite having only one mobile ionic species, in certain circumstances two characteristic timescales of ionic motion in the perovskite can be observed. These arise if the transport layer bands are misaligned, as in the three-feature spectra modelled in Section 2.2, and the density of one of the charge carrier species becomes sufficiently high to lead to a carrier Debye length (Λ_n for electrons and Λ_p for holes) that is comparable to (or smaller than) b , the width of the PAL. The carrier Debye lengths are defined as

$$\Lambda_n = \sqrt{\frac{V_T \varepsilon_p}{q d_E k_E}}, \quad \Lambda_p = \sqrt{\frac{V_T \varepsilon_p}{q d_H k_H}}, \quad (4)$$

where V_T is the thermal voltage, ε_p is the permittivity of the PAL, q is the elementary charge, d is the effective doping density of the respective transport layer and k is a constant associated with the transport layer-PAL band offset defined in (S17). In such circumstances, the carriers can partially screen the field from the interior of the PAL and a small excess of ions flows into the PAL bulk in response to the relatively large carrier densities in an attempt to re-establish charge neutrality. The timescale τ_2 for the motion of this small excess of ions turns out to be a key timescale of the problem, the other key timescale being τ_1 , which is that for ions to migrate into and out of the Debye layer on the edge of the PAL. The latter (as described in [52]) is given by

$$\tau_1 = \frac{\Lambda_P b}{D_P}, \quad (5)$$

where Λ_P is the ionic Debye length, defined as

$$\Lambda_P = \sqrt{\frac{V_T \varepsilon_p}{q N_0}}, \quad (6)$$

N_0 is the average density of mobile ions, and D_P is the ionic diffusion coefficient. In order to estimate τ_2 we note that the excess ions flow into the bulk from one of the boundary layers (to re-establish charge

neutrality) through a drift-dominated ion flux F_P of the order of $\frac{D_P N_0}{b}$. Assuming that electrons, with a typical density n_0 , are the dominant charge-carrier species, the size of the ionic excess in the bulk ($P - N_0$) is also n_0 and, given the estimate of the ion flux F_P above, we can estimate the timescale τ_2 , for the motion of the excess ions across the PAL as

$$\tau_2 = \frac{n_0 b^2}{N_0 D_P}. \quad (7)$$

As has been noted by Bennett *et al.* [53], the slow τ_1 timescale is associated with the low-frequency feature in the impedance spectrum. The newly identified timescale τ_2 is associated with any mid-frequency feature that appears. The high frequency feature, as discussed in [53], is independent of ion motion, being a consequence of the interplay of displacement currents and charge carrier recombination currents. The ratio of the frequencies at which LF and MF features appear is therefore

$$\frac{f_{MF}}{f_{LF}} \approx \frac{N_0 \Lambda_P}{n_0 b} \quad (8)$$

where $f_{LF} = 1/\tau_1$ and $f_{MF} = 1/\tau_2$. For a third impedance feature to appear, the ionic Debye length must be much smaller than the perovskite layer ($\Lambda_P/b \ll 1$) and the ratio of $\frac{n_0}{N_0}$ must be approximately $(\Lambda_P/b)^2$ under the assumptions of the mSPM. For an ionic Debye length of $\Lambda_P = 1.5$ nm [52] and a PAL thickness of $b = 300$ nm, the reduced order model predicts the MF feature to appear at frequencies approximately 200 times larger than that of the LF, in excellent agreement with the full drift-diffusion simulations. Note that this argument is easily generalised to the case where holes are the dominant electronic carrier species rather than electrons.

3.3.2 Ultra-low frequencies

At the very lowest frequencies, the drift-diffusion model predicts that the entire system remains in equilibrium with the AC voltage. Ion vacancies migrate into/out of the thin layers at each side of the PAL, fully screening the electric field in the bulk, as shown in Figure 16a. At the peaks of the AC voltage, additional electronic carriers enter the PAL from the transport layers but the electronic charge is much smaller than the ion vacancy density in the bulk, meaning it is easily neutralised by a small density of excess mobile ions, supplied by the thin boundary layers. As the entire system has time to equilibrate with the AC voltage, there is no phase delay and thus no imaginary component to the impedance.

3.3.3 Low frequencies

The low frequency (LF) regime refers here to frequencies of $f \approx 1/\tau_1$ where τ_1 is the characteristic timescale for ion migration into/out of the space charge layers (5). As shown in Figure 16b, the AC voltage begins to oscillate fast enough that the ions cannot charge/discharge the space charge layers quickly enough to screen the bulk from the electric field. The charge/discharge of the thin space charge layers on either side of the PAL begins to lag behind the AC voltage, introducing a phase delay to the system. This phase delay in the bulk electric field modulates the electronic carrier densities, which in turn affect the recombination rate, and leads to a phase delay in the current flowing through the device. This manifests itself as an imaginary component of the impedance.

Whilst the ions residing in the space charge layers near the transport layer interfaces cannot respond quickly enough to the LF voltage oscillations driving the system that they remain in phase with them, the small density of excess ions in the PAL bulk can re-establish charge neutrality there on a timescale approximately 200 times faster than the ions in the space charge layers. The electric potential in the PAL bulk thus remains linear and the LF behaviour does not differ from that observed in the standard SPM [53].

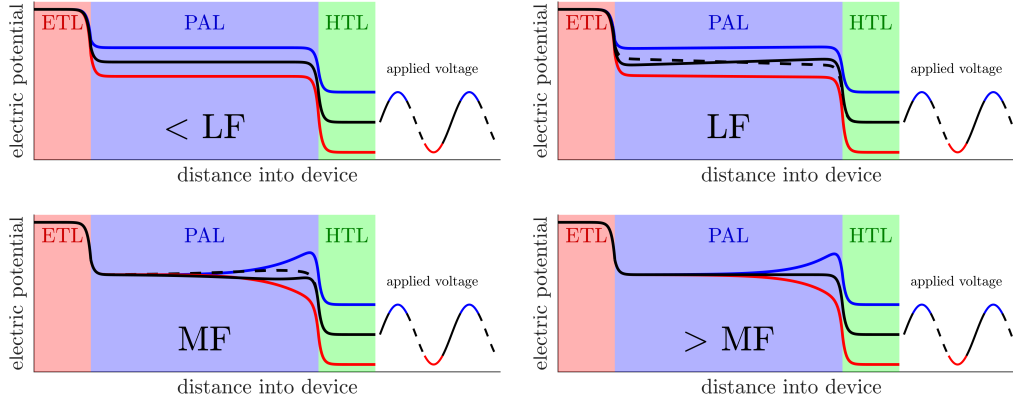


Figure 16: Electric potential in each frequency regime. Impedance features occur when the black dashed line does not coincide with the black solid line, *i.e.* the electric potential has a phase delay. Note that oscillations are greatly exaggerated in these illustrative plots. In this example, the ETL-perovskite band offset is small. Corresponding plots for the densities of electrons, holes and mobile ions can be found in Section 4 of the supplementary information.

3.3.4 Mid frequencies

In the mid frequency (MF) regime ($f \approx 1/\tau_2$), the behaviour of the mSPM diverges significantly from that of the standard SPM. At mid frequencies, the space charge layers on either side of the PAL are ‘frozen in’, no longer able to respond to the AC voltage. As discussed above, the small population of excess ions in the PAL can equilibrate on a much faster timescale than that of the ions in the thin boundary layers. Thus it is only at mid frequencies that these excess ions begin to lag behind the AC voltage. Whilst the electronic carriers equilibrate with the electric potential almost instantaneously, the excess ions move too slowly to fully screen the charge within the bulk, as shown in Figure 16c. There exists a range of frequencies at which the excess ions can respond partially but not fully to the AC voltage, causing the electric potential to exhibit wavelike behaviour in the bulk (see video in Supplementary Information). In this scenario, the bulk electrical potential, and thus carrier densities and recombination, experience a phase delay relative to the AC voltage, resulting in an imaginary component of impedance and a mid frequency feature on the Nyquist plot.

3.3.5 High frequencies

The excess ions are finally ‘frozen in’ in the high frequency (HF) regime, $f \gg 1/\tau_2$ where the frequency of the forcing voltage is so high that the ions are unable to respond to it. With mobile ions ‘frozen in’ across all layers, the only charge transport occurring on these timescales is the injection/extraction of electronic carriers from the transport layers into the PAL bulk. The bulk therefore oscillates between being net positively charged and net negatively charged. At all practical experimental frequencies, electronic carrier motion can be assumed to occur instantaneously such that, while the electric potential in the bulk is nonlinear, it is in phase with the AC voltage (as depicted in Figure 16d).

As briefly mentioned above, the high-frequency limit of the capacitance in the mSPM is not solely from the geometric capacitance. In scenarios where carrier densities in the PAL are very large (devices with high carrier leakage), their Debye length becomes similar to the layer thickness, allowing them to partially screen the field. When this happens, an electronic capacitance is present as well as the geometric. The measured capacitance at high frequencies (typically MHz) is

$$C_{\text{HF}} = \frac{\epsilon_p}{\Lambda} \frac{e^{2b/\Lambda} + 1}{e^{2b/\Lambda} - 1} \quad (9)$$

where Λ is the Debye length of the dominant carrier in the PAL. As shown in the supplementary

information (Section 1.8), this reduces to the geometric capacitance when both carrier Debye lengths are much greater than the layer width $\Lambda \gg b$.

3.3.6 Sign of the LF and MF impedance features

As seen in the numerical simulations presented in Section 2, the four classes of three-feature spectra are created by the signs of the LF and MF feature, where each can be either positive or negative. Here we explain the necessary conditions for both of these features to be positive or negative, beginning with the low frequency feature.

It was found by Bennett *et al.* that the sign of the low frequency feature under SRH bulk recombination is determined by the potential differences between the perovskite and the transport layers at the DC voltage [53]. The LF feature is negative if $|\phi_{\text{HTL}} - \phi_{\text{PAL}}| > |\phi_{\text{ETL}} - \phi_{\text{PAL}}|$ and recombination is hole-limited, or if $|\phi_{\text{ETL}} - \phi_{\text{PAL}}| > |\phi_{\text{HTL}} - \phi_{\text{PAL}}|$ and recombination is electron-limited, and positive otherwise. At low frequencies, the excess ions in the mSPM fully screen the bulk charge, meaning the LF feature is still described by this behaviour. We also note that, for DC voltages near the built-in voltage (within approximately 5 thermal voltages), this amounts to a negative LF feature if $\varepsilon_H d_H < \varepsilon_E d_E$ and recombination is hole-limited or if $\varepsilon_H d_H > \varepsilon_E d_E$ and recombination is electron-limited, and positive otherwise; here ε and d are the permittivity and effective doping density, respectively, of the transport layers. The conditions in which the LF feature is positive or negative are summarised in Table 2.



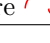
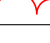
| electric potential condition | bulk recombination type | |
|---|--|--|
| | electron-limited | hole-limited |
| $ \phi_{\text{HTL}} - \phi_{\text{PAL}} > \phi_{\text{ETL}} - \phi_{\text{PAL}} $ | positive LF feature  | negative LF feature  |
| $ \phi_{\text{ETL}} - \phi_{\text{PAL}} > \phi_{\text{HTL}} - \phi_{\text{PAL}} $ | negative LF feature  | positive LF feature  |

Table 2: Summary of the conditions that produce a positive or negative low-frequency impedance feature.

The sign of the mid frequency feature depends only on the majority carrier in the PAL (caused by a low band offset and/or higher doping density) and the recombination type. If recombination is limited by the majority carrier the MF feature is negative (Figures 12 and 13), otherwise it is positive (Figures 11 and 14). It is worth remarking that the signs of neither the LF nor the MF features are directly dependent on device architecture (*i.e.* direction of incident light). However, the different material choices required for p-i-n and n-i-p cells may well affect the signs of the LF and MF features through indirect means such as permittivity and band offset.

4 Discussion

4.1 Diagnostic capabilities of the model

It has often been remarked that three-feature spectra are more commonly found in lower efficiency cells. The mSPM not only explains the reason for this correlation but also provides a diagnostic pathway that can help to identify the source of efficiency losses and the material changes that may increase performance in future. Table 3 lists the six classes of PSC impedance spectra discussed in this work, alongside the conditions required to produce them, provided by the mSPM. In addition to the conclusions drawn regarding two-feature spectra by Bennett *et al.* [53], the appearance of a third feature indicates that the density of either electrons or holes is large in the perovskite at the DC voltage, such that the mobile ion density in the bulk is displaced from its equilibrium value. Furthermore, the recombination rate is likely dominated by bulk SRH, as a third feature can only be induced under surface recombination when electronic carrier densities in the perovskite are unrealistically large. The sign of the MF feature is determined by the recombination-limiting carrier and the large-density carrier in the bulk.


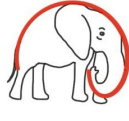
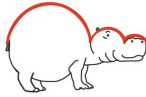


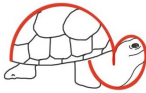
| Name | Shape | Cell information | |
|----------|---|---|--|
| | | if $d_H \varepsilon_H > d_E \varepsilon_E$ | if $d_E \varepsilon_E > d_H \varepsilon_H$ |
| ladybird |  | <ul style="list-style-type: none"> • Either recombination is bulk SRH dominated and electron and hole densities are very small OR recombination is surface SRH dominated | |
| elephant |  | <ul style="list-style-type: none"> • Electron and hole densities in the perovskite are very small • Recombination dominated by hole-limited bulk SRH | <ul style="list-style-type: none"> • Electron and hole densities in the perovskite are very small • Recombination dominated by electron-limited bulk SRH |
| hippo |  | <ul style="list-style-type: none"> • Hole density in the perovskite is large • Recombination dominated by electron-limited bulk SRH | <ul style="list-style-type: none"> • Electron density in the perovskite is large • Recombination dominated by hole-limited bulk SRH |
| manatee |  | <ul style="list-style-type: none"> • Hole density in the perovskite is large • Recombination dominated by hole-limited bulk SRH | <ul style="list-style-type: none"> • Electron density in the perovskite is large • Recombination dominated by electron-limited bulk SRH |
| rabbit |  | <ul style="list-style-type: none"> • Electron density in the perovskite is large • Recombination dominated by electron-limited bulk SRH | <ul style="list-style-type: none"> • Hole density in the perovskite is large • Recombination dominated by hole-limited bulk SRH |
| tortoise |  | <ul style="list-style-type: none"> • Electron density in the perovskite is large • Recombination dominated by hole-limited bulk SRH | <ul style="list-style-type: none"> • Hole density in the perovskite is large • Recombination dominated by electron-limited bulk SRH |

Table 3: Summary of the necessary conditions for the drift-diffusion model to recreate each of the six categories of two- or three-feature spectra. Here d denotes the effective doping density (*i.e.* the equilibrium carrier density) and ε the permittivity. A subscript E or H corresponds to the ETL or HTL, respectively.

Three-feature impedance spectra are an indication that a significant density of one of the carrier species accumulates in the perovskite bulk at the DC voltage of the experiment and, consequently, that one of the charge transport layers performs poorly at this voltage; that is it does not efficiently extract carriers from the perovskite layer before they recombine. We hypothesise that the most likely cause of this poor carrier extraction efficiency is an insufficient band offset between the perovskite and transport layers, and suggest searching for an alternative transport material.

4.2 Comparison with experiment

As discussed in Section 2, all four classes of three-feature spectra are usually observed at large DC voltages, at or near maximum power point (MPP) and open-circuit, when the cell is illuminated. This is consistent with the predictions of the mSPM which suggest that a large voltage is necessary in order to induce a mid-frequency feature. The electron (hole) density in the perovskite bulk at the DC voltage is exponentially dependent on the potential difference between the perovskite bulk and the centre of the ETL (HTL). At a DC voltage much smaller than the built-in voltage, carrier densities in the perovskite bulk become very small, meaning that ion vacancies are not displaced from the perovskite bulk in significant numbers and the behaviour of the standard SPM is recovered. Conversely, at voltages much larger than the built-in voltage, carrier densities in the bulk can become large and, depending on other material parameters such as band offsets, may displace ion vacancies from the bulk in sufficient numbers to result in a significant ion vacancy excess (or deficit) and hence induce a mid frequency feature. This suggests that mid-frequency features are unlikely to be observed at small DC voltages, approaching short-circuit.

In an effort to gather more information about the LF and MF features, Pering and Cameron performed impedance spectroscopy experiments across a range of temperatures [31,65]. The temperature dependence of the characteristic timescale associated with each arc can be used to fit an activation energy and an attempt frequency. It was concluded that the activation energies of the LF and MF features were similar and both consistent with iodide ion vacancy migration. Conversely, the attempt frequency was typically found to be 1-2 orders of magnitude higher for the MF feature (10^{10} - 10^{11} s⁻¹) than the LF (10^9 - 10^{10} s⁻¹). Based on this observation they concluded that the features were caused by iodide ions in two different environments (e.g. at the grain boundary and in the bulk) that were responding to the applied field on two different timescales. Here we show that the features can be explained by a single ionic species in two different environments, namely within the space charge layers or in the perovskite bulk.

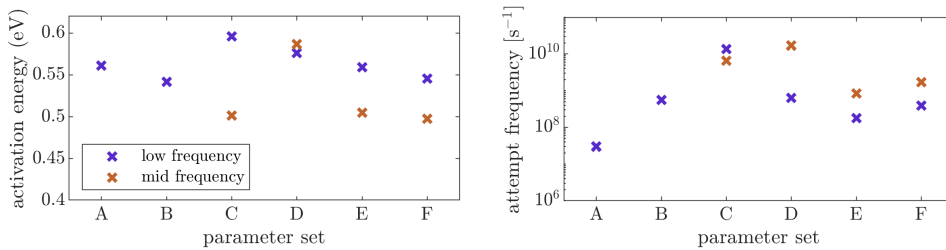


Figure 17: Activation energies and attempt frequencies for the six parameter sets listed in Table S1. Values calculated from impedance spectra obtained through the reduced order model (17) described in Section 3.3.

The drift-diffusion model accounts for temperature changes by scaling the thermal voltage and modifying the ion vacancy diffusion coefficient according to

$$D_P = D_\infty \exp\left(\frac{-E_a}{k_B T}\right) \quad (10)$$

where D_∞ and E_a are the high-temperature diffusion coefficient and activation energy, respectively. In line with [21] we set the ionic activation energy in all simulations to be

$$E_a = 0.58 \text{ eV} \quad \text{in all simulations} \quad (11)$$

and selected D_∞ in each parameter set to be such that the room-temperature diffusion coefficients listed in Table S1 were attained at 298 K. Once again, we note that some groups have suggested the vacancy activation energy should be lower than this value [98], but reducing the activation energy does not affect the proposed mechanism underlying the MF features and our conclusions are thus unchanged. The activation energies and attempt frequencies of the LF and MF features, computed from simulations using the mSPM across a range of temperatures, are shown in Figure 17. We find that, with one exception in each case, both sets of results show the following similarities with the experimental data reported by Pering and Cameron [31]. Activation energies for the two impedance features are similar, with that of the MF appearing slightly lower than the LF, and attempt frequencies are typically 1-2 orders of magnitude higher for the MF feature than the LF. The exact process by which the activation energies in the impedance spectrum are modified from E_a in the DD model is still unclear and deserves further investigation, as do the reason for the difference between the LF and MF activation energies and the material parameters that determine the measured attempt frequencies in the DD model. Despite this, it is encouraging that this detailed analysis shows strong similarities between the temperature dependence of the modelled results and the experimentally observed temperature dependence. The measurement of impedance spectra at different temperatures remains an important method for extracting activation energies and diffusion coefficients for the mobile ionic species in perovskite devices.

4.3 Possible future experiments

Whilst the drift and diffusion of a single mobile ionic species, coupled to that of two charge carrier species, can explain many of the three-feature spectra reported in the literature, it is not the only candidate hypothesis, although it is probably the simplest. Other hypotheses, such as faster ionic migration along grain boundaries [31], have been proposed as the cause of MF impedance features. Here we discuss potential future experiments that may be used to distinguish between alternative hypotheses.

As discussed briefly in Section 4.2, measuring the effect of changes in temperature on the impedance response offers additional information. Specifically the activation energy and attempt frequency that can be extracted from each impedance feature can be tested against the predictions of competing theories. While this characterisation technique has not been widely adopted, it can be performed relatively easily and adds a new dimension to the reported data.

Alternatively, this theory could be tested by using different materials to alter the band structure of the device. We predict that the large accumulation of holes or electrons in the perovskite bulk is due to an insufficient band offset between the perovskite and the relevant transport layer. Thus, selecting materials such that the band offset is increased should cause the MF feature to disappear from the spectrum. One route to achieving this is to use a series of different (or differently doped) transport layers in order to vary the band offset. This does however impact other aspects of the cell, such as the built-in voltage, meaning other changes to the spectrum may be observed as well. Alternatively, ion substitutions could be used to vary the band gap of the perovskite. The results from simulating this experiment are shown in Figure 18, in which the increased band gap shows the complete removal of the MF impedance feature. This may prove difficult in practice as the ionic substitutions are likely to alter other material properties, such as recombination sites and it is not obvious which band (or indeed both) the increased band gap will shift. While some studies [39, 83, 99] have looked at the effect of altering band offsets in the device, through material substitution, the impedance response is a function of the band picture throughout the entire device and thus depends on other variables, such as built-in voltage.

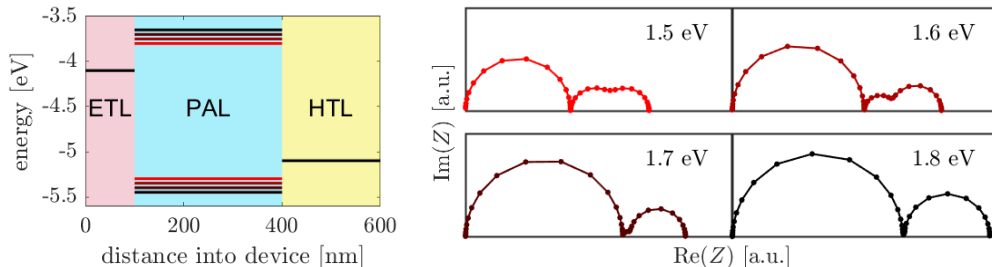


Figure 18: A proposed experiment to test the theory of bulk excess ion movement as a cause of three-feature spectra. Left panel shows device band structures, with the corresponding simulated Nyquist plots shown in the right panels, obtained from simulation of the drift-diffusion model (S1-S17) in IonMonger. As the perovskite band gap is increased from 1.5eV to 1.8eV (for example, by ion substitution) so are the band offsets, reducing the carrier densities in the perovskite and thus the density of the compensating excess ions.

4.4 Best practices for reporting PSC impedance spectroscopy

The modelling presented here highlights some potential pitfalls when interpreting impedance data from PSCs. Here we discuss strategies to avoid these and suggested practices for minimising confusion in the reporting of these data.

Many impedance spectra in the literature are only measured at frequencies above 1 Hz, partly due to the long time required for low frequency measurements, but also because of the poor stability of some perovskite devices during long term measurements. Ideally all impedance spectra would be measured to 0.1mHz or lower to allow the clearest interpretation of the results. As discussed in Section 3, the ion-induced mid- and low-frequency features bear many similarities when viewed in isolation. The large range in reported values of the ion vacancy diffusion coefficient means it is likely that one cell may well exhibit a LF feature at frequencies where another cell is in the MF regime. By only measuring frequencies above 1 Hz, it can be difficult to distinguish whether the second arc is a true LF feature or a MF feature with an unseen impedance response lying at lower frequencies. In order to successfully measure EIS data below 1Hz it is necessary to ensure that the cell is stable over these timescales, since anomalous features may be observed if the cell parameters start drifting as a result of degradation occurring on the timescale of the measurement.¹ It is usually helpful to carry out a Kramers-Kronig analysis of the low frequency data to ensure that the results are reliable. To illustrate the problems incomplete data can pose when modelling the data, we consider the example of the Nyquist plot shown in Figure 19a, reported by Hernandez *et al.* [28]. The Nyquist plot appears to show a single ‘LF’ feature but it is not fully resolved before the 1 Hz cut-off. There are thus two possible ways to reconstruct this shape from the DD model. The first is to treat this as a true LF feature, appearing above 1 Hz (as depicted in Figure 19, center panel) and the second is to assume that this is actually a MF feature, caused by bulk excess ion motion, and that the true LF feature lies below 1 Hz (as depicted in Figure 19, right panel). While both approaches successfully recreate the Nyquist plot, the ambiguity in the data leads to significant differences in parameter fits (most notably the band edges and ion diffusion coefficient) and therefore also in the overall interpretation of cell performance.

This point is emphasised in Figure 20, in which the approximate boundaries between the frequency regimes are plotted for different values of the vacancy diffusion coefficient (D_P). With a 1 Hz cut-off, the mid frequency regime is only fully resolved if $D_P \geq 10^{-16} \text{ m}^2 \text{ s}^{-1}$. Similarly, the low frequency

¹While cell degradation during measurement is often cited as a possible cause of unusual PSC spectra, here we focus on the wide variety of shapes that can be obtained from stable cells that do not degrade during measurements. Preliminary work suggests that the shapes of the Nyquist plots can be affected by degradation. This is something that we will address fully in future work.

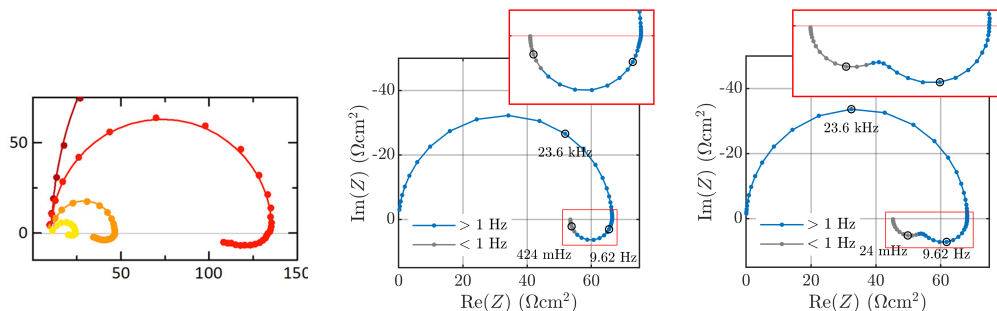


Figure 19: The difficulties of modelling incomplete spectra. The left panel shows a measured impedance spectrum reported by Hernandez *et al.* [28] (reproduced under CC-BY 4.0). The negative region could be interpreted as either a true LF feature (modelled in centre panel) or a MF feature with an unseen LF feature lying below the cut-off frequency (modelled in right panel). Centre and right panels obtained from simulation of the drift-diffusion model (S1-S17) in IonMonger, using parameter sets G1 and G2, respectively, listed in Table S1.

regime is likely only well-resolved if $D_P \geq 10^{-14} \text{ m}^2 \text{ s}^{-1}$. Given an estimated diffusion coefficient of $D_P = 10^{-16} \text{ m}^2 \text{ s}^{-1}$ for iodide vacancies in MAPI [21], we expect these experiments to capture only the MF feature, and not the LF.

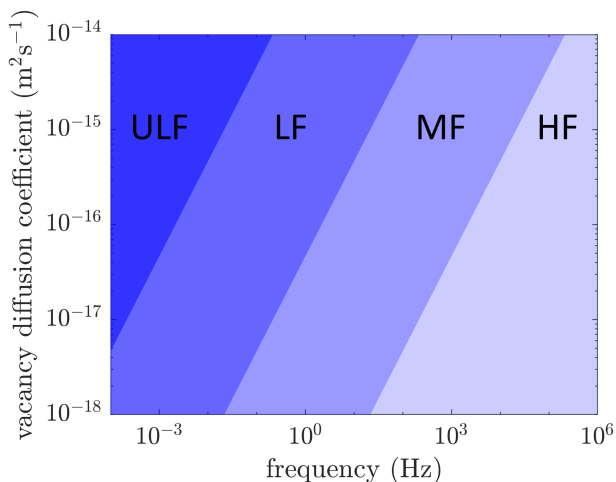


Figure 20: Approximate boundaries between frequency regimes as a function of ion vacancy diffusion coefficient. Based on assumptions of perovskite permittivity $24.1\epsilon_0$, PAL width 400nm, temperature 298K and mean ion vacancy density 10^{26} m^{-3} .

In efforts to minimise the confusion resulting from these measurements, it is crucial that reported Nyquist plots include labelled frequencies (see, for example, Figure 11b) and clearly communicate the frequency range present in the data. Furthermore, authors should comment on the possibility of unresolved lower frequency features and limitations of the characterisation process where appropriate.

5 Conclusions

It has previously been speculated that impedance spectra of PSCs showing more than two features are anomalous and are perhaps caused by non-steady state measurement conditions or cell degradation

during measurement. We have shown here, however, that a third impedance feature is a natural consequence of the standard ionic-electronic drift-diffusion model of a PSC in certain parameter regimes. Furthermore, we have employed a reduced order model, which accurately approximates solutions to the DD model, that is capable of isolating the exact conditions in which this third feature can appear. When large densities of electrons or holes are present in the perovskite at the DC voltage, the mobile ions are displaced slightly such that their density is not equal to that of the static background ionic charge in the bulk. This effectively creates a small population of ‘excess ions’ which act to neutralise small electronic charges in the perovskite layer over timescales approximately 200 times faster than the ion migration into and out of the thin space charge layers at the perovskite/transport layer interfaces. At mid frequencies, the excess ions can only partially respond to the electronic charge, which results in a phase delay. An ion-modulated recombination rate in the perovskite bulk therefore induces the mid frequency feature. Furthermore, we have shown that these large densities of carriers in the perovskite can increase the observed capacitance relative to the geometric capacitance, contrary to previous interpretation of the high-frequency impedance feature. As briefly discussed in Section 2.2.1, we have only shown each spectrum at a single DC voltage, chosen to replicate the experimental conditions in which each shape was observed and give the best resolution of the impedance features. In reality, the shape of the Nyquist plot for a cell depends on several factors, including the DC voltage and illumination intensity. Work on modelling and understanding PSC impedance spectra throughout the voltage-illumination plane is underway.

Unlike the phenomenological equivalent circuit models used elsewhere to interpret the impedance response of a PSC, the drift-diffusion model that we employ here is a physics-based model with the advantage that all input parameters have a clear, well-defined physical interpretation. Solutions to the modified Surface Polarisation Model (mSPM), which accurately approximate those to the drift-diffusion model, allow us to predict the band offsets and dominant types of recombination from the observed shape of the impedance spectrum of a PSC.

Finally, we have discussed best practices for performing and reporting impedance measurements in order to aid meaningful interpretation of data and avoid potential pitfalls. In particular, it is important that, where possible, low frequency measurements are made and, if not, that the cut-off frequency is clearly stated.

The analysis presented here leads to a diagnostic framework that may be used to locate performance losses in cells that exhibit three-feature spectra (summarised in Table 3). The qualitative shape of the Nyquist plot is sufficient to provide information about both densities of electrons and holes in the perovskite layer and the dominant source of recombination, offering valuable insights into future device optimisation.

Acknowledgements

WC was supported by an EPSRC grant (reference EP/V520056/1). The authors wish to thank Imogen Tozer for her illustrations. The authors have no competing financial interests to declare.

Data availability statement

All simulations were produced using the parameter sets listed in the supplementary information and the freely available open-access software IonMonger².

Appendix: The reduced order model

The reduced order model, referred to as the modified surface polarisation model (mSPM) is systematically derived from the full drift-diffusion model (S1-S17) by Clarke *et al.* [25] and stated as follows.

²<https://github.com/PerovskiteSCModelling/IonMonger>

| Symbol | Definition |
|-----------------------|-------------------------------------|
| D_P | ion vacancy diffusion coefficient |
| V_{bi} | built-in voltage |
| $V(t)$ | applied voltage |
| V_T | thermal voltage |
| q | the elementary charge |
| N_0 | average ion vacancy density |
| $\varepsilon_{E/p/H}$ | permittivity of ETL/PAL/HTL |
| $d_{E/H}$ | effective doping density of ETL/HTL |

Table 4: Symbols employed in the modified surface polarisation model (12).

The electric potential in the PAL bulk $\phi(x, t)$ is governed by a partial differential equation

$$\frac{\Lambda_P^2}{D_P} \frac{\partial}{\partial t} \left[\frac{1}{\Lambda_n^2} \exp\left(\frac{\phi - \frac{V_{bi}-V}{2}}{V_T}\right) - \frac{1}{\Lambda_p^2} \exp\left(\frac{-\phi - \frac{V_{bi}-V}{2}}{V_T}\right) - \frac{1}{V_T} \frac{\partial^2 \phi}{\partial x^2} \right] = \frac{1}{V_T} \frac{\partial^2 \phi}{\partial x^2}, \quad (12a)$$

coupled to two ordinary differential equations governing the ionic charge density in the thin layers either side of the bulk ($\mathcal{Q}_L(t)$ and $\mathcal{Q}_R(t)$),

$$\frac{d\mathcal{Q}_L}{dt} = \frac{qD_P N_0}{V_T} \frac{\partial \phi}{\partial x} \Big|_{x=0}, \quad \frac{d\mathcal{Q}_R}{dt} = -\frac{qD_P N_0}{V_T} \frac{\partial \phi}{\partial x} \Big|_{x=b}, \quad (12b)$$

via boundary conditions

$$\phi|_{x=0} = \frac{V_{bi} - V(t)}{2} - V_1 - V_2, \quad \phi|_{x=b} = -\frac{V_{bi} - V(t)}{2} + V_3 + V_4. \quad (12c)$$

The four boundary layer potentials $V_{1,\dots,4}$ are functions of \mathcal{Q}_L and \mathcal{Q}_R :

$$V_1 = -V_T \mathcal{V} \left(\frac{\mathcal{Q}_L}{\sqrt{q\varepsilon_E d_E V_T}} \right), \quad V_2 = -V_T \mathcal{V} \left(\frac{\mathcal{Q}_L}{\sqrt{q\varepsilon_p N_0 V_T}} \right), \quad (12d)$$

$$V_3 = V_T \mathcal{V} \left(\frac{\mathcal{Q}_R}{\sqrt{q\varepsilon_p N_0 V_T}} \right), \quad V_4 = -V_T \mathcal{V} \left(-\frac{\mathcal{Q}_R}{\sqrt{q\varepsilon_H d_H V_T}} \right), \quad (12e)$$

using a nonlinear capacitance relation $\mathcal{V}(\mathcal{Q})$, being the inverse of

$$\mathcal{Q}(\mathcal{V}) = \text{sign}(\mathcal{V}) \sqrt{2(e^{\mathcal{V}} - \mathcal{V} - 1)}. \quad (13)$$

Material parameters used in this model are listed in Table 4 and $\Lambda_{P,n,p}$ are the Debye lengths defined in (4) and (6). The current density can be calculated on this background electric potential by solving the following boundary value problem for the electron and hole current densities (j^n and j^p):

$$\frac{dj^n}{dx} = -q(G - R), \quad j^n|_{x=b} = -qR_r, \quad (14)$$

$$\frac{dj^p}{dx} = q(G - R), \quad j^p|_{x=0} = -qR_l. \quad (15)$$

In order to obtain the impedance, this model is linearised in terms of a small perturbation to the voltage with frequency ω :

$$V(t) = V_{DC} + V_p \sin(\omega t). \quad (16)$$

The leading order current response to this perturbation under various recombination pathways is derived in the electronic supplementary information, arriving at an analytic expression $Z(\omega)$ for the impedance response as a function of frequency:

$$Z(\omega) = \frac{-V_T}{\mathcal{J}_R + \mathcal{J}_d}, \quad (17)$$

where \mathcal{J}_R and \mathcal{J}_d are complex functions of ω arising from the AC recombination current (S63) and displacement current (S64), respectively.

References

- [1] Akihiro Kojima, Kenjiro Teshima, Tsutomu Miyasaka, and Yasuo Shirai. Novel photoelectrochemical cell with mesoscopic electrodes sensitized by lead-halide compounds (2). In *ECS Meeting Abstracts*, page 397. IOP Publishing, 2006.
- [2] Akihiro Kojima, Kenjiro Teshima, Yasuo Shirai, and Tsutomu Miyasaka. Organometal halide perovskites as visible-light sensitizers for photovoltaic cells. *Journal of the american chemical society*, 131(17):6050–6051, 2009.
- [3] James M. Ball, Michael M. Lee, Andrew Hey, and Henry J. Snaith. Low-temperature processed meso-superstructured to thin-film perovskite solar cells. *Energy & Environmental Science*, 6(6):1739, 2013.
- [4] NREL. Best research-cell efficiency chart, <https://www.nrel.gov/pv/cell-efficiency.html> (accessed 30/10/2023). <https://www.nrel.gov/pv/cell-efficiency.html>. Accessed type = Web Page.
- [5] Felix Lang, Oleksandra Shargaieva, Viktor V. Brus, Heinz C. Neitzert, Jörg Rappich, et al. Influence of radiation on the properties and the stability of hybrid perovskites. *Advanced Materials*, 30(3):1702905, 2018.
- [6] Sang-Won Lee, Seongtak Kim, Soohyun Bae, Kyungjin Cho, Taewon Chung, et al. Uv degradation and recovery of perovskite solar cells. *Scientific Reports*, 6(1):38150, 2016.
- [7] Nam-Koo Kim, Young Hwan Min, Seokhwan Noh, Eunkyung Cho, Gitaeg Jeong, et al. Investigation of thermally induced degradation in CH₃NH₃PbI₃ perovskite solar cells using in-situ synchrotron radiation analysis. *Scientific Reports*, 7(1), 2017.
- [8] Philippe Holzhey, Pankaj Yadav, Silver-Hamill Turren-Cruz, Amita Ummadisingu, Michael Grätzel, et al. A chain is as strong as its weakest link—stability study of MAPbI₃ under light and temperature. *Materials Today*, 29:10–19, 2019.
- [9] Jonas A. Schwenzler, Lucija Rakocevic, Robert Gehlhaar, Tobias Abzieher, Saba Gharibzadeh, et al. Temperature variation-induced performance decline of perovskite solar cells. *ACS Applied Materials & Interfaces*, 10(19):16390–16399, 2018.
- [10] Daniel Bryant, Nicholas Aristidou, Sebastian Pont, Irene Sanchez-Molina, Thana Chotchunangatchaval, et al. Light and oxygen induced degradation limits the operational stability of methylammonium lead triiodide perovskite solar cells. *Energy & Environmental Science*, 9(5):1655–1660, 2016.
- [11] Jinli Yang, Braden D. Siempelkamp, Dianyi Liu, and Timothy L. Kelly. Investigation of CH₃NH₃PbI₃ degradation rates and mechanisms in controlled humidity environments using in situ techniques. *ACS Nano*, 9(2):1955–1963, 2015.

- [12] John M. Howard, Elizabeth M. Tennyson, Sabyasachi Barik, Rodrigo Szostak, Edo Waks, et al. Humidity-induced photoluminescence hysteresis in variable cs/br ratio hybrid perovskites. *The Journal of Physical Chemistry Letters*, 9(12):3463–3469, 2018.
- [13] Mark V. Khenkin, Anoop K. M, Eugene A. Katz, and Iris Visoly-Fisher. Bias-dependent degradation of various solar cells: lessons for stability of perovskite photovoltaics. *Energy & Environmental Science*, 12(2):550–558, 2019.
- [14] Konrad Domanski, Bart Roose, Taisuke Matsui, Michael Saliba, Silver-Hamill Turren-Cruz, et al. Migration of cations induces reversible performance losses over day/night cycling in perovskite solar cells. *Energy & Environmental Science*, 10(2):604–613, 2017.
- [15] Yongbo Yuan and Jinsong Huang. Ion migration in organometal trihalide perovskite and its impact on photovoltaic efficiency and stability. *Accounts of Chemical Research*, 49(2):286–293, 2016.
- [16] Felix Utama Kosasih and Caterina Ducati. Characterising degradation of perovskite solar cells through in-situ and operando electron microscopy. *Nano Energy*, 47:243–256, 2018.
- [17] Antonio Abate. Perovskite solar cells go lead free. *Joule*, 1(4):659–664, 2017.
- [18] Zhen Li, Xin Wu, Shengfan Wu, Danpeng Gao, Hua Dong, et al. An effective and economical encapsulation method for trapping lead leakage in rigid and flexible perovskite photovoltaics. *Nano Energy*, 93:106853, 2022.
- [19] Yan Jiang, Longbin Qiu, Emilio J. Juarez-Perez, Luis K. Ono, Zhanhao Hu, et al. Reduction of lead leakage from damaged lead halide perovskite solar modules using self-healing polymer-based encapsulation. *Nature Energy*, 4(7):585–593, 2019.
- [20] Shangshang Chen, Yehao Deng, Xun Xiao, Shuang Xu, Peter N. Rudd, et al. Preventing lead leakage with built-in resin layers for sustainable perovskite solar cells. *Nature Sustainability*, 4(7):636–643, 2021.
- [21] Christopher Eames, Jarvist M. Frost, Piers R. F. Barnes, Brian C. O’Regan, Aron Walsh, et al. Ionic transport in hybrid lead iodide perovskite solar cells. *Nature Communications*, 6(1):7497, 2015.
- [22] Davide Moia, Ilario Gelmetti, Phil Calado, William Fisher, Michael Stringer, Onkar Game, Yinghong Hu, Pablo Docampo, David Lidzey, Emilio Palomares, Jenny Nelson, and Piers R. F. Barnes. Ionic-to-electronic current amplification in hybrid perovskite solar cells: ionically gated transistor-interface circuit model explains hysteresis and impedance of mixed conducting devices. *Energy & Environmental Science*, 12(4):1296–1308, 2019.
- [23] Henry J. Snaith, Antonio Abate, James M. Ball, Giles E. Eperon, Tomas Leijtens, et al. Anomalous hysteresis in perovskite solar cells. *The Journal of Physical Chemistry Letters*, 5(9):1511–1515, 2014.
- [24] Eva Lisa Unger, Eric T Hoke, Colin D Bailie, William H Nguyen, Andrea Ruth Bowring, T Heumüller, Mark Greyson Christoforo, and Michael D McGehee. Hysteresis and transient behavior in current–voltage measurements of hybrid-perovskite absorber solar cells. *Energy & Environmental Science*, 7(11):3690–3698, 2014.
- [25] Will Clarke, Matthew V Cowley, Matthew J Wolf, Petra Cameron, Alison Walker, and Giles Richardson. Inverted hysteresis as a diagnostic tool for perovskite solar cells: Insights from the drift-diffusion model. *Journal of Applied Physics*, 133(9):095001, 2023.

- [26] Nathan S Hill, Matthew V Cowley, Nadja Gluck, Miriam H Fsadni, Will Clarke, Yinghong Hu, Matthew J Wolf, Noel Healy, Marina Freitag, and Thomas J Penfold. Ionic accumulation as a diagnostic tool in perovskite solar cells: Characterizing band alignment with rapid voltage pulses. *Advanced Materials*, 35(32):2302146, 2023.
- [27] Victoria Gonzalez-Pedro, Emilio J Juarez-Perez, Waode-Sukmawati Arsyad, Eva M Barea, Francisco Fabregat-Santiago, Ivan Mora-Sero, and Juan Bisquert. General working principles of $\text{ch}_3\text{nh}_3\text{pbx}_3$ perovskite solar cells. *Nano letters*, 14(2):888–893, 2014.
- [28] Enrique Hernández-Balaguera and Juan Bisquert. Negative transient spikes in halide perovskites. *ACS Energy Letters*, 7(8):2602–2610, 2022.
- [29] Itaru Raifuku, Yasuaki Ishikawa, Seigo Ito, and Yukiharu Uraoka. Characteristics of perovskite solar cells under low-illuminance conditions. *The Journal of Physical Chemistry C*, 120(34):18986–18990, 2016.
- [30] Elena Guillén, F Javier Ramos, Juan A Anta, and Shahzada Ahmad. Elucidating transport-recombination mechanisms in perovskite solar cells by small-perturbation techniques. *The Journal of Physical Chemistry C*, 118(40):22913–22922, 2014.
- [31] Samuel R Pering and Petra J Cameron. The effect of multiple ion substitutions on halide ion migration in perovskite solar cells. *Materials Advances*, 3(21):7918–7924, 2022.
- [32] Antonio Guerrero, Juan Bisquert, and Germà Garcia-Belmonte. Impedance spectroscopy of metal halide perovskite solar cells from the perspective of equivalent circuits. *Chemical Reviews*, 121(23):14430–14484, 2021.
- [33] Firouzeh Ebadi, Nima Taghavinia, Raheleh Mohammadpour, Anders Hagfeldt, and Wolfgang Tress. Origin of apparent light-enhanced and negative capacitance in perovskite solar cells. *Nature communications*, 10(1):1574, 2019.
- [34] Agustin O. Alvarez, Ramón Arcas, Clara A. Aranda, Loengrid Bethencourt, Elena Mas-Marzá, Michael Saliba, and Francisco Fabregat-Santiago. Negative capacitance and inverted hysteresis: Matching features in perovskite solar cells. *The Journal of Physical Chemistry Letters*, 11(19):8417–8423, 2020.
- [35] Juan Bisquert, Antonio Guerrero, and Cedric Gonzales. Theory of hysteresis in halide perovskites by integration of the equivalent circuit. *ACS Physical Chemistry Au*, 1(1):25–44, 2021.
- [36] Ilaria Maticena, Pierluigi Guerriero, Laura Lancellotti, Brigida Alfano, Antonella De Maria, Vera La Ferrara, Lucia V Mercaldo, Maria Lucia Miglietta, Tiziana Polichetti, and Gabriella Rametta. Impedance spectroscopy analysis of perovskite solar cell stability. *Energies*, 16(13):4951, 2023.
- [37] Jie Zhang and Thierry Pauporté. Effects of oxide contact layer on the preparation and properties of $\text{ch}_3\text{nh}_3\text{pbi}_3$ for perovskite solar cell application. *The Journal of Physical Chemistry C*, 119(27):14919–14928, 2015.
- [38] Haimang Yi, Dian Wang, Leiping Duan, Faiazul Haque, Cheng Xu, Yu Zhang, Gavin Conibeer, and Ashraf Uddin. Solution-processed wo_3 and water-free pedot : Pss composite for hole transport layer in conventional perovskite solar cell. *Electrochimica Acta*, 319:349–358, 2019.
- [39] Antonio Guerrero, Germà Garcia-Belmonte, Ivan Mora-Sero, Juan Bisquert, Yong Soo Kang, T Jesper Jacobsson, Juan-Pablo Correa-Baena, and Anders Hagfeldt. Properties of contact and bulk impedances in hybrid lead halide perovskite solar cells including inductive loop elements. *The Journal of Physical Chemistry C*, 120(15):8023–8032, 2016.

- [40] Francisco Fabregat-Santiago, Michael Kulbak, Arava Zohar, Marta Vallés-Pelarda, Gary Hodes, David Cahen, and Ivan Mora-Sero. Deleterious effect of negative capacitance on the performance of halide perovskite solar cells. *ACS Energy Letters*, 2(9):2007–2013, 2017.
- [41] Maria Ulfa, Pengjiu Wang, Jie Zhang, Jiawen Liu, Willy Daney de Marcillac, Laurent Coolen, Sebastien Peralta, and Thierry Pauporte. Charge injection and electrical response in low-temperature SnO_2 -based efficient perovskite solar cells. *ACS applied materials & interfaces*, 10(41):35118–35128, 2018.
- [42] Naemeh Aeineh, Eva M Barea, Abbas Behjat, Nafiseh Sharifi, and Iván Mora-Seró. Inorganic surface engineering to enhance perovskite solar cell efficiency. *ACS Applied Materials & Interfaces*, 9(15):13181–13187, 2017.
- [43] Pankaj Yadav, Daniel Prochowicz, Michael Saliba, Pablo P Boix, Shaik M Zakeeruddin, and Michael Grätzel. Interfacial kinetics of efficient perovskite solar cells. *Crystals*, 7(8):252, 2017.
- [44] Hua Zhang, Xianfeng Qiao, Yan Shen, Thomas Moehl, Shaik M Zakeeruddin, Michael Grätzel, and Mingkui Wang. Photovoltaic behaviour of lead methylammonium triiodide perovskite solar cells down to 80 K. *Journal of Materials Chemistry A*, 3(22):11762–11767, 2015.
- [45] Qian-Qian Chu, Zhijian Sun, Bin Ding, Kyoung-sik Moon, Guan-Jun Yang, and Ching-Ping Wong. Greatly enhanced power conversion efficiency of hole-transport-layer-free perovskite solar cell via coherent interfaces of perovskite and carbon layers. *Nano Energy*, 77:105110, 2020.
- [46] Loreta A Muscarella, Yulia Galagan, Simon Christian Boehme, and Elizabeth von Hauff. Trap passivation and suppressed electrochemical dynamics in perovskite solar cells with C_{60} interlayers. *Electrochimica Acta*, 433:141215, 2022.
- [47] Pengjiu Wang, Zhipeng Shao, Maria Ulfa, and Thierry Pauporté. Insights into the hole blocking layer effect on the perovskite solar cell performance and impedance response. *The Journal of Physical Chemistry C*, 121(17):9131–9141, 2017.
- [48] Elnaz Ghahremanirad, Agustín Bou, Saeed Olyaei, and Juan Bisquert. Inductive loop in the impedance response of perovskite solar cells explained by surface polarization model. *The Journal of Physical Chemistry Letters*, 8(7):1402–1406, 2017.
- [49] Fedros Galatopoulos, Achilleas Savva, Ioannis T Papadas, and Stelios A Choulis. The effect of hole transporting layer in charge accumulation properties of pin perovskite solar cells. *APL Materials*, 5(7), 2017.
- [50] Maria Ulfa, Tao Zhu, Fabrice Goubard, and Thierry Pauporté. Molecular versus polymeric hole transporting materials for perovskite solar cell application. *Journal of Materials Chemistry A*, 6(27):13350–13358, 2018.
- [51] Lidia Contreras-Bernal, Susana Ramos-Terrón, Antonio Riquelme, Pablo P Boix, Jesús Idígoras, Iván Mora-Seró, and Juan A Anta. Impedance analysis of perovskite solar cells: a case study. *Journal of Materials Chemistry A*, 7(19):12191–12200, 2019.
- [52] Giles Richardson, Simon E. J. O’Kane, Ralf G. Niemann, Timo A. Peltola, Jamie M. Foster, et al. Can slow-moving ions explain hysteresis in the current–voltage curves of perovskite solar cells? *Energy & Environmental Science*, 9(4):1476–1485, 2016.
- [53] Laurence J. Bennett, Antonio J. Riquelme, Juan A. Anta, Nicola E. Courtier, and Giles Richardson. Avoiding ionic interference in computing the ideality factor for perovskite solar cells and an analytical theory of their impedance-spectroscopy response. *Physical Review Applied*, 19(1), 2023.

- [54] N. E. Courtier, G. Richardson, and J. M. Foster. A fast and robust numerical scheme for solving models of charge carrier transport and ion vacancy motion in perovskite solar cells. *Applied Mathematical Modelling*, 63:329–348, 2018.
- [55] Antonio Riquelme, Laurence J. Bennett, Nicola E. Courtier, Matthew J. Wolf, Lidia Contreras-Bernal, et al. Identification of recombination losses and charge collection efficiency in a perovskite solar cell by comparing impedance response to a drift-diffusion model. *Nanoscale*, 12(33):17385–17398, 2020.
- [56] Martin T. Neukom, Andreas Schiller, Simon Züfle, Evelyne Knapp, Jorge Ávila, et al. Consistent device simulation model describing perovskite solar cells in steady-state, transient, and frequency domain. *ACS Applied Materials & Interfaces*, 11(26):23320–23328, 2019.
- [57] Daniel A Jacobs, Heping Shen, Florian Pfeffer, Jun Peng, Thomas P White, Fiona J Beck, and Kylie R Catchpole. The two faces of capacitance: New interpretations for electrical impedance measurements of perovskite solar cells and their relation to hysteresis. *Journal of Applied Physics*, 124(22), 2018.
- [58] N. E. Courtier, J. M. Foster, S. E. J. O’Kane, A. B. Walker, and G. Richardson. Systematic derivation of a surface polarisation model for planar perovskite solar cells. *European Journal of Applied Mathematics*, 30(3):427–457, 2019.
- [59] Nicola E. Courtier, James M. Cave, Jamie M. Foster, Alison B. Walker, and Giles Richardson. How transport layer properties affect perovskite solar cell performance: insights from a coupled charge transport/ion migration model. *Energy & Environmental Science*, 12(1):396–409, 2019.
- [60] N. E. Courtier, J. M. Cave, A. B. Walker, G. Richardson, and J. M. Foster. Ionmonger: a free and fast planar perovskite solar cell simulator with coupled ion vacancy and charge carrier dynamics. *Journal of Computational Electronics*, 18(4):1435–1449, 2019.
- [61] Will Clarke, Laurence J. Bennett, Yoana Grudeva, Jamie M. Foster, Giles Richardson, and Nicola E. Courtier. Ionmonger 2.0: software for free, fast and versatile simulation of current, voltage and impedance response of planar perovskite solar cells. *Journal of Computational Electronics*, 2022.
- [62] Adam Pockett, Giles E Eperon, Timo Peltola, Henry J Snaith, Alison Walker, Laurence M Peter, and Petra J Cameron. Characterization of planar lead halide perovskite solar cells by impedance spectroscopy, open-circuit photovoltage decay, and intensity-modulated photovoltage/photocurrent spectroscopy. *The Journal of Physical Chemistry C*, 119(7):3456–3465, 2015.
- [63] Ganga R Neupane, Matthew Bamidele, Vishal Yeddu, Do Young Kim, and Parameswar Hari. Negative capacitance and hysteresis in encapsulated mapbi3 and lead–tin (pb–sn) perovskite solar cells. *Journal of Materials Research*, 37(7):1357–1372, 2022.
- [64] Junke Wang, Yulia Galagan, and Elizabeth von Hauff. Quantifying electrochemical losses in perovskite solar cells. *Journal of Materials Chemistry C*, 11(8):2911–2920, 2023.
- [65] Adam Pockett, Giles E Eperon, Nobuya Sakai, Henry J Snaith, Laurence M Peter, and Petra J Cameron. Microseconds, milliseconds and seconds: deconvoluting the dynamic behaviour of planar perovskite solar cells. *Physical Chemistry Chemical Physics*, 19(8):5959–5970, 2017.
- [66] Sandheep Ravishankar, Clara Aranda, Sandy Sanchez, Juan Bisquert, Michael Saliba, and Germà Garcia-Belmonte. Perovskite solar cell modeling using light-and voltage-modulated techniques. *The Journal of Physical Chemistry C*, 123(11):6444–6449, 2019.

- [67] Amna Bashir, Jia Haur Lew, Sudhanshu Shukla, Disha Gupta, Tom Baikie, Sudip Chakraborty, Rahul Patidar, Annalisa Bruno, Subodh Mhaisalkar, and Zareen Akhter. Cu-doped nickel oxide interface layer with nanoscale thickness for efficient and highly stable printable carbon-based perovskite solar cell. *Solar Energy*, 182:225–236, 2019.
- [68] Mustafa KA Mohammed. 21.4% efficiency of perovskite solar cells using bmimi additive in the lead iodide precursor based on carbon nanotubes/tio2 electron transfer layer. *Ceramics International*, 46(17):27647–27654, 2020.
- [69] Govindhasamy Murugadoss, Hiroyuki Kanda, Soichiro Tanaka, Hitoshi Nishino, Seigo Ito, Hiroshi Imahori, and Tomokazu Umeyama. An efficient electron transport material of tin oxide for planar structure perovskite solar cells. *Journal of Power Sources*, 307:891–897, 2016.
- [70] Fuguo Zhang, Xichuan Yang, Ming Cheng, Weihang Wang, and Licheng Sun. Boosting the efficiency and the stability of low cost perovskite solar cells by using cupc nanorods as hole transport material and carbon as counter electrode. *Nano Energy*, 20:108–116, 2016.
- [71] Mohammad Mahdi Tavakoli, Pankaj Yadav, Rouhollah Tavakoli, and Jing Kong. Surface engineering of tio2 etl for highly efficient and hysteresis-less planar perovskite solar cell (21.4%) with enhanced open-circuit voltage and stability. *Advanced Energy Materials*, 8(23):1800794, 2018.
- [72] Dianyi Liu, Jinli Yang, and Timothy L Kelly. Compact layer free perovskite solar cells with 13.5% efficiency. *Journal of the American Chemical Society*, 136(49):17116–17122, 2014.
- [73] Zubair Ahmad, Arti Mishra, Sumayya Muhammad Abdulrahim, and Farid Touati. Electrical equivalent circuit (eec) based impedance spectroscopy analysis of htm free perovskite solar cells. *Journal of Electroanalytical Chemistry*, 871:114294, 2020.
- [74] Liujin Lin, Chenjie Gu, Juye Zhu, Qiufeng Ye, Ershuai Jiang, Wei Wang, Mingdun Liao, Zhenhai Yang, Yuheng Zeng, and Jiang Sheng. Engineering of hole-selective contact for high-performance perovskite solar cell featuring silver back-electrode. *Journal of Materials Science*, 54:7789–7797, 2019.
- [75] Alexander R Pascoe, Noel W Duffy, Andrew D Scully, Fuzhi Huang, and Yi-Bing Cheng. Insights into planar ch₃nh₃pb₃ perovskite solar cells using impedance spectroscopy. *The Journal of Physical Chemistry C*, 119(9):4444–4453, 2015.
- [76] Kenjiro Miyano, Neeti Tripathi, Masatoshi Yanagida, and Yasuhiro Shirai. Lead halide perovskite photovoltaic as a model p–i–n diode. *Accounts of chemical research*, 49(2):303–310, 2016.
- [77] Hui-Seon Kim, Ivan Mora-Sero, Victoria Gonzalez-Pedro, Francisco Fabregat-Santiago, Emilio J Juarez-Perez, Nam-Gyu Park, and Juan Bisquert. Mechanism of carrier accumulation in perovskite thin-absorber solar cells. *Nature communications*, 4(1):2242, 2013.
- [78] Emilio J Juarez-Perez, Rafael S Sanchez, Laura Badia, Germá Garcia-Belmonte, Yong Soo Kang, Ivan Mora-Sero, and Juan Bisquert. Photoinduced giant dielectric constant in lead halide perovskite solar cells. *The journal of physical chemistry letters*, 5(13):2390–2394, 2014.
- [79] Monojit Bag, Lawrence A Renna, Ramesh Y Adhikari, Supravat Karak, Feng Liu, Paul M Lahti, Thomas P Russell, Mark T Tuominen, and D Venkataraman. Kinetics of ion transport in perovskite active layers and its implications for active layer stability. *Journal of the American Chemical Society*, 137(40):13130–13137, 2015.
- [80] Stijn Lammar, Renán Escalante, Antonio J Riquelme, Sandra Jenatsch, Beat Ruhstaller, Gerko Oskam, Tom Aernouts, and Juan A Anta. Impact of non-stoichiometry on ion migration and photovoltaic performance of formamidinium-based perovskite solar cells. *Journal of Materials Chemistry A*, 10(36):18782–18791, 2022.

- [81] Cedric Gonzales, Antonio Guerrero, and Juan Bisquert. Transition from capacitive to inductive hysteresis: A neuron-style model to correlate $i-v$ curves to impedances of metal halide perovskites. *The Journal of Physical Chemistry C*, 126(32):13560–13578, 2022.
- [82] Rodrigo García-Rodríguez, Dominic Ferdani, Samuel Pering, Peter J Baker, and Petra J Cameron. Influence of bromide content on iodide migration in inverted MAPb(I_{1-x}Br_x)₃ perovskite solar cells. *Journal of Materials Chemistry A*, 7(39):22604–22614, 2019.
- [83] Varun Srivastava, Akhil Alexander, B. Anitha, and Manoj A. G. Namboothiry. Impedance spectroscopy study of defect/ion mediated electric field and its effect on the photovoltaic performance of perovskite solar cells based on different active layers. *Solar Energy Materials and Solar Cells*, 237:111548, 2022.
- [84] Ik Jae Park, Jae Hyun Park, Su Geun Ji, Min-Ah Park, Ju Hee Jang, and Jin Young Kim. A three-terminal monolithic perovskite/si tandem solar cell characterization platform. *Joule*, 3(3):807–818, 2019.
- [85] Agustín Bou, Adam Pockett, Dimitrios Raptis, Trystan Watson, Matthew J Carnie, and Juan Bisquert. Beyond impedance spectroscopy of perovskite solar cells: Insights from the spectral correlation of the electrooptical frequency techniques. *The Journal of Physical Chemistry Letters*, 11(20):8654–8659, 2020.
- [86] Anna Todinova, Lidia Contreras-Bernal, Manuel Salado, Shahzada Ahmad, Neftalí Morillo, Jesús Idígoras, and Juan A. Anta. Towards a universal approach for the analysis of impedance spectra of perovskite solar cells: Equivalent circuits and empirical analysis. *ChemElectroChem*, 4(11):2891–2901, 2017.
- [87] Yulin Feng, Jiming Bian, Minhuan Wang, Shi Wang, Chunyang Zhang, Qingshun Dong, Bingye Zhang, and Yantao Shi. Interfacial negative capacitance in planar perovskite solar cells: an interpretation based on band theory. *Materials Research Bulletin*, 107:74–79, 2018.
- [88] F Javier Ramos, Maria C López-Santos, Elena Guillén, Mohammad Khaja Nazeeruddin, Michael Grätzel, Agustín R Gonzalez-Elipé, and Shahzada Ahmad. Perovskite solar cells based on nanocolumnar plasma-deposited zno thin films. *ChemPhysChem*, 15(6):1148–1153, 2014.
- [89] Antonio Guerrero, Agustín Bou, Gebhard Matt, Osbel Almora, Thomas Heumüller, Germà Garcia-Belmonte, Juan Bisquert, Yi Hou, and Christoph Brabec. Switching off hysteresis in perovskite solar cells by fine-tuning energy levels of extraction layers. *Advanced Energy Materials*, 8(21):1703376, 2018.
- [90] Philip Calado, Ilario Gelmetti, Benjamin Hilton, Mohammed Azzouzi, Jenny Nelson, and Piers R. F. Barnes. Driftfusion: an open source code for simulating ordered semiconductor devices with mixed ionic-electronic conducting materials in one dimension. *Journal of Computational Electronics*, 2022.
- [91] Philip Calado, Andrew M. Telford, Daniel Bryant, Xiaoe Li, Jenny Nelson, Brian C. O’Regan, and Piers R. F. Barnes. Evidence for ion migration in hybrid perovskite solar cells with minimal hysteresis. *Nature Communications*, 7(1):13831, 2016.
- [92] Nir Tessler and Yana Vaynzof. Insights from device modeling of perovskite solar cells. *ACS Energy Letters*, 5(4):1260–1270, 2020.
- [93] Dilara Abdel, Petr Vágner, Jürgen Fuhrmann, and Patricio Farrell. Modelling charge transport in perovskite solar cells: Potential-based and limiting ion depletion. *Electrochimica Acta*, 390:138696, 2021.

- [94] Alejandra Castro-Chong, Antonio J. Riquelme, Tom Aernouts, Laurence J. Bennett, Giles Richardson, et al. Illumination intensity dependence of the recombination mechanism in mixed perovskite solar cells. *ChemPlusChem*, 86(9):1347–1356, 2021.
- [95] Luca Bertoluzzi, Caleb C. Boyd, Nicholas Rolston, Jixian Xu, Rohit Prasanna, Brian C. O’Regan, and Michael D. McGehee. Mobile ion concentration measurement and open-access band diagram simulation platform for halide perovskite solar cells. *Joule*, 4(1):109–127, 2020.
- [96] Aron Walsh, David O. Scanlon, Shiyu Chen, X. G. Gong, and Su-Huai Wei. Self-regulation mechanism for charged point defects in hybrid halide perovskites. *Angewandte Chemie*, 127(6):1811–1814, 2015.
- [97] Samuel G McCallum, Oliver Nicholls, Kjeld O Jensen, Matthew V Cowley, James E Lerpinière, and Alison B Walker. Bayesian parameter estimation for characterising mobile ion vacancies in perovskite solar cells. *Journal of Physics: Energy*, 6(1):015005, 2023.
- [98] Juan Antonio Seijas-Bellido, Bipasa Samanta, Karen Valadez-Villalobos, Juan Jesús Gallardo, Javier Navas, Salvador R. G. Balestra, Rafael María Madero Castro, José Manuel Vicent-Luna, Shuxia Tao, Maytal Caspary Toroker, and Juan Antonio Anta. Transferable classical force field for pure and mixed metal halide perovskites parameterized from first-principles. *Journal of Chemical Information and Modeling*, 62(24):6423–6435, 2022.
- [99] Osbel Almora, Kyung Taek Cho, Sadig Aghazada, Iwan Zimmermann, Gebhard J. Matt, Christoph J. Brabec, Mohammad Khaja Nazeeruddin, and Germà Garcia-Belmonte. Discerning recombination mechanisms and ideality factors through impedance analysis of high-efficiency perovskite solar cells. *Nano Energy*, 48:63–72, 2018.

Electronic supplementary information

1 Derivation of the approximate solutions to the drift-diffusion model

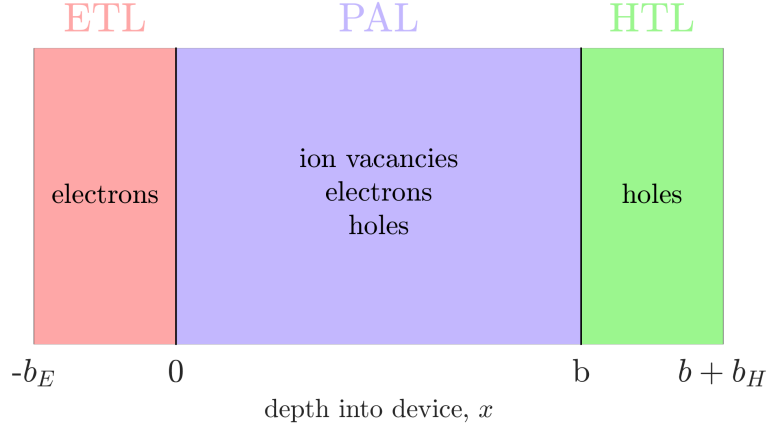


Figure S1: Schematic of the drift-diffusion model, showing the mobile charged species modelled in each layer.

1.1 Drift-diffusion model

The full three-layer drift-diffusion model, adopting the notation of Courtier *et al.* [60].

Perovskite layer ($0 \leq x \leq b$)

$$\frac{\partial P}{\partial t} + \frac{\partial F^P}{\partial x} = 0, \quad F^P = -D_P \left(\frac{\partial P}{\partial x} + \frac{P}{V_T} \frac{\partial \phi}{\partial x} \right), \quad (\text{S1})$$

$$\frac{\partial n}{\partial t} - \frac{1}{q} \frac{\partial j^n}{\partial x} = G(x, t) - R(n, p), \quad j^n = qD_n \left(\frac{\partial n}{\partial x} - \frac{n}{V_T} \frac{\partial \phi}{\partial x} \right), \quad (\text{S2})$$

$$\frac{\partial p}{\partial t} + \frac{1}{q} \frac{\partial j^p}{\partial x} = G(x, t) - R(n, p), \quad j^p = -qD_p \left(\frac{\partial p}{\partial x} + \frac{p}{V_T} \frac{\partial \phi}{\partial x} \right), \quad (\text{S3})$$

$$\frac{\partial^2 \phi}{\partial x^2} = \frac{q}{\varepsilon_p} (N_0 - P + n - p). \quad (\text{S4})$$

Electron transport layer ($-b_E < x < 0$)

$$\frac{\partial n}{\partial t} - \frac{1}{q} \frac{\partial j^n}{\partial x} = 0, \quad j^n = qD_E \left(\frac{\partial n}{\partial x} - \frac{n}{V_T} \frac{\partial \phi}{\partial x} \right), \quad \frac{\partial^2 \phi}{\partial x^2} = \frac{q}{\varepsilon_E} (n - d_E), \quad (\text{S5})$$

Hole transport layer ($b < x < b + b_H$)

$$\frac{\partial p}{\partial t} + \frac{1}{q} \frac{\partial j^p}{\partial x} = 0, \quad j^p = -qD_H \left(\frac{\partial p}{\partial x} + \frac{p}{V_T} \frac{\partial \phi}{\partial x} \right), \quad \frac{\partial^2 \phi}{\partial x^2} = \frac{q}{\varepsilon_H} (d_H - p), \quad (\text{S6})$$

Boundary conditions

$$F^P|_{x=0} = 0, \quad F^P|_{x=b} = 0, \quad (\text{S7})$$

$$j^P|_{x=0^+} = -qR_l(n|_{x=0^-}, p|_{x=0^+}), \quad j^n|_{x=b^-} = -qR_r(n|_{x=b^-}, p|_{x=b^+}), \quad (\text{S8})$$

$$n|_{x=-b_E} = d_E, \quad p|_{x=b+b_H} = d_H, \quad (\text{S9})$$

$$\phi|_{x=-b_E} = \frac{V_{bi} - V(t)}{2}, \quad \phi|_{x=b+b_H} = -\frac{V_{bi} - V(t)}{2}. \quad (\text{S10})$$

Continuity conditions

$$n|_{x=0^+} = k_E n|_{x=0^-}, \quad (\text{S11})$$

$$p|_{x=b^-} = k_H p|_{x=b^+}, \quad (\text{S12})$$

$$\phi|_{x=0^-} = \phi|_{x=0^+}, \quad \phi|_{x=b^-} = \phi|_{x=b^+}, \quad (\text{S13})$$

$$\varepsilon_E \frac{\partial \phi}{\partial x} \Big|_{x=0^-} = \varepsilon_P \frac{\partial \phi}{\partial x} \Big|_{x=0^+}, \quad \varepsilon_P \frac{\partial \phi}{\partial x} \Big|_{x=b^-} = \varepsilon_H \frac{\partial \phi}{\partial x} \Big|_{x=b^+}, \quad (\text{S14})$$

$$j^n|_{x=0^-} = j^n|_{x=0^+} - R_l(n|_{x=0^-}, p|_{x=0^+}), \quad (\text{S15})$$

$$j^p|_{x=b^-} = j^p|_{x=b^+} + R_r(n|_{x=b^-}, p|_{x=b^+}), \quad (\text{S16})$$

where

$$k_E = \frac{g_c}{g_c^E} \exp\left(\frac{E_c^E - E_c}{k_B T}\right), \quad k_H = \frac{g_v}{g_v^H} \exp\left(\frac{E_v - E_v^H}{k_B T}\right). \quad (\text{S17})$$

1.2 The modified surface polarisation model

The modified surface polarisation model (mSPM) is an asymptotic simplification of the full DD model, derived by Clarke *et al.* [25], based on the assumptions of the surface polarisation model (SPM) [59] tweaked to allow large carrier densities in the perovskite bulk to impact the ionic distribution. The electric potential is determined by a PDE in the perovskite bulk coupled to two ODEs for ionic boundary layer charge density:

$$\frac{1}{V_T} \frac{\partial^2 \phi}{\partial x^2} = \frac{\Lambda_P^2}{D_P} \frac{\partial}{\partial t} \left[\frac{1}{\Lambda_n^2} \exp\left(\frac{\phi - \frac{V_{bi} - V(t)}{2}}{V_T}\right) - \frac{1}{\Lambda_p^2} \exp\left(\frac{-\phi - \frac{V_{bi} - V(t)}{2}}{V_T}\right) - \frac{1}{V_T} \frac{\partial^2 \phi}{\partial x^2} \right] \quad (\text{S18a})$$

$$\frac{dQ_L}{dt} = \frac{qD_P N_0}{V_T} \frac{\partial \phi}{\partial x} \Big|_{x=0}, \quad (\text{S18b})$$

$$\frac{dQ_R}{dt} = -\frac{qD_P N_0}{V_T} \frac{\partial \phi}{\partial x} \Big|_{x=b}, \quad (\text{S18c})$$

where Λ_P , Λ_n and Λ_p are the Debye lengths of ion vacancies, electrons and holes, respectively, in the perovskite, defined in (4) and (6). The appropriate boundary conditions for this model are

$$\phi|_{x=0} = -\frac{V(t) - V_{bi}}{2} - V_1 - V_2, \quad \phi|_{x=b} = \frac{V(t) - V_{bi}}{2} + V_3 + V_4, \quad (\text{S18d})$$

where the four boundary layer potentials ($V_{1,\dots,4}$, see Figure S2) are determined by the two ionic charge densities (Q_L and Q_R) via the following nonlinear capacitance relations:

$$V_1 = -V_T \mathcal{V}\left(\frac{Q_L}{\sqrt{q\varepsilon_E d_E V_T}}\right), \quad V_2 = -V_T \mathcal{V}\left(\frac{Q_L}{\sqrt{q\varepsilon_P N_0 V_T}}\right), \quad (\text{S18e})$$

$$V_3 = V_T \mathcal{V}\left(\frac{Q_R}{\sqrt{q\varepsilon_P N_0 V_T}}\right), \quad V_4 = -V_T \mathcal{V}\left(-\frac{Q_R}{\sqrt{q\varepsilon_H d_H V_T}}\right), \quad (\text{S18f})$$

where the DC boundary layer voltages are given in terms of the DC surface charge densities by

$$V_1^{\text{DC}} = -V_T \mathcal{V} \left(\frac{Q_L^{\text{DC}}}{\sqrt{q\varepsilon_E d_E V_T}} \right), \quad V_2^{\text{DC}} = -V_T \mathcal{V} \left(\frac{Q_L^{\text{DC}}}{\sqrt{q\varepsilon_p N_0 V_T}} \right), \quad (\text{S23})$$

$$V_3^{\text{DC}} = V_T \mathcal{V} \left(\frac{Q_R^{\text{DC}}}{\sqrt{q\varepsilon_p N_0 V_T}} \right), \quad V_4^{\text{DC}} = -V_T \mathcal{V} \left(-\frac{Q_R^{\text{DC}}}{\sqrt{q\varepsilon_H d_H V_T}} \right). \quad (\text{S24})$$

The final condition needed to solve the DC problem is a statement of ionic conservation: $\int_0^b P dx = N_0 b$. In the formalism of the mSPM, this becomes

$$Q_L^{\text{DC}} + Q_R^{\text{DC}} = qb \left[d_H k_H e^{-\frac{V_3^{\text{DC}} - V_4^{\text{DC}}}{V_T}} - d_E k_E e^{-\frac{V_1^{\text{DC}} - V_2^{\text{DC}}}{V_T}} \right], \quad (\text{S25})$$

where the right hand terms represent the density of excess ions that enter/leave the PAL bulk in response to the electronic charge. Note that in most circumstances (when the DC voltage is near V_{bi}) the RHS will be approximately zero. In equations (S22)-(S25) we have seven equations with which to determine the seven unknowns ϕ^{DC} , V_1^{DC} , V_2^{DC} , V_3^{DC} , V_4^{DC} , Q_L^{DC} and Q_R^{DC} in terms of V^{DC} .

1.4 Linearising the electric potential problem

The DC solution is perturbed by an oscillating voltage:

$$V(t) = V^{\text{DC}} + \delta V_T e^{i\omega t} \quad (\text{S26})$$

where δ (the magnitude of the perturbation in units of thermal voltages) is small and ω is the **angular** frequency of the perturbation. The three variables present in the electric potential problem are linearised in terms of the magnitude of the perturbation:

$$\phi(x, t) = \phi^{\text{DC}} + \delta \phi^{\text{AC}}, \quad Q_L(t) = Q_L^{\text{DC}} + \delta Q_L^{\text{AC}}, \quad Q_R(t) = Q_R^{\text{DC}} + \delta Q_R^{\text{AC}}. \quad (\text{S27})$$

After substituting these expansions into the mSPM (S18), the zeroth order terms (in δ) recover the DC steady state problem and the first order terms determine the AC problem:

$$D_P \frac{\partial^2 \phi^{\text{AC}}}{\partial x^2} = \frac{n^{\text{DC}}}{N_0} \left(\frac{\partial \phi^{\text{AC}}}{\partial t} + \frac{i\omega V_T}{2} e^{i\omega t} \right) + \frac{p^{\text{DC}}}{N_0} \left(\frac{\partial \phi^{\text{AC}}}{\partial t} - \frac{i\omega V_T}{2} e^{i\omega t} \right) - \Lambda_P^2 \frac{\partial}{\partial t} \frac{\partial^2 \phi^{\text{AC}}}{\partial x^2}, \quad (\text{S28})$$

$$\frac{dQ_L^{\text{AC}}}{dt} = \frac{qD_P N_0}{V_T} \frac{\partial \phi^{\text{AC}}}{\partial x} \Big|_{x=0}, \quad (\text{S29})$$

$$\frac{dQ_R^{\text{AC}}}{dt} = -\frac{qD_P N_0}{V_T} \frac{\partial \phi^{\text{AC}}}{\partial x} \Big|_{x=b}, \quad (\text{S30})$$

with boundary conditions

$$\phi^{\text{AC}}|_{x=0} = \frac{-V_T}{2} e^{i\omega t} - V_1^{\text{AC}} - V_2^{\text{AC}} \quad \phi^{\text{AC}}|_{x=b} = \frac{V_T}{2} e^{i\omega t} + V_3^{\text{AC}} + V_4^{\text{AC}}. \quad (\text{S31})$$

Here we have expanded the boundary layer potentials as $V_i = V_i^{\text{DC}} + \delta V_i^{\text{AC}}$ and linearised the boundary layer capacitance relations to obtain

$$V_1^{\text{AC}} = -\chi_1 Q_L^{\text{AC}}, \quad V_2^{\text{AC}} = -\chi_2 Q_L^{\text{AC}}, \quad V_3^{\text{AC}} = \chi_3 Q_R^{\text{AC}}, \quad V_4^{\text{AC}} = \chi_4 Q_R^{\text{AC}}, \quad (\text{S32})$$

where

$$\chi_1 = \sqrt{\frac{V_T}{q\varepsilon_E d_E}} \frac{d\mathcal{V}}{d\mathcal{Q}} \Big|_{\mathcal{Q}=\frac{Q_L^{\text{DC}}}{\sqrt{q\varepsilon_E d_E V_T}}}, \quad \chi_2 = \sqrt{\frac{V_T}{q\varepsilon_p N_0}} \frac{d\mathcal{V}}{d\mathcal{Q}} \Big|_{\mathcal{Q}=\frac{Q_L^{\text{DC}}}{\sqrt{q\varepsilon_p N_0 V_T}}}, \quad (\text{S33})$$

$$\chi_3 = \sqrt{\frac{V_T}{q\varepsilon_p N_0}} \frac{d\mathcal{V}}{d\mathcal{Q}} \Big|_{\mathcal{Q}=\frac{Q_R^{\text{DC}}}{\sqrt{q\varepsilon_p N_0 V_T}}}, \quad \chi_4 = \sqrt{\frac{V_T}{q\varepsilon_H d_H}} \frac{d\mathcal{V}}{d\mathcal{Q}} \Big|_{\mathcal{Q}=\frac{-Q_R^{\text{DC}}}{\sqrt{q\varepsilon_H d_H V_T}}}, \quad (\text{S34})$$

are constants determined by the DC steady state.

1.5 Periodic solutions for electric potential

Impedance measurements rely on the assumption that the system has reached a periodic quasi-equilibrium with angular frequency ω . We therefore restrict solutions to be of the form

$$\phi^{\text{AC}} = f(x)e^{i\omega t}, \quad Q_L^{\text{AC}} = Ae^{i\omega t}, \quad Q_R^{\text{AC}} = Be^{i\omega t}. \quad (\text{S35})$$

Substituting these solutions into the electric potential PDE (S18a) gives an ordinary differential equation for f :

$$f''(x) - \frac{i\omega(n^{\text{DC}} + p^{\text{DC}})}{N_0(D_P + i\omega\Lambda_P^2)}f(x) = \frac{1}{2} \frac{i\omega V_T(n^{\text{DC}} - p^{\text{DC}})}{N_0(D_P + i\omega\Lambda_P^2)} \quad (\text{S36})$$

which is generally solved by

$$f(x) = Ce^{zx} + De^{z(b-x)} + V_T F \quad (\text{S37})$$

where

$$z = \sqrt{\frac{\omega(n^{\text{DC}} + p^{\text{DC}})(\omega\Lambda_P^2 + iD_P)}{N_0(D_P^2 + \omega^2\Lambda_P^4)}}, \quad F = \frac{p^{\text{DC}} - n^{\text{DC}}}{2(p^{\text{DC}} + n^{\text{DC}})}, \quad (\text{S38})$$

and C and D are unknown. Note that

$$F \approx \begin{cases} \frac{1}{2} & \text{if } p^{\text{DC}} \gg n^{\text{DC}}, \\ -\frac{1}{2} & \text{if } p^{\text{DC}} \ll n^{\text{DC}}. \end{cases} \quad (\text{S39})$$

Applying the boundary conditions (S18) to ϕ gives

$$(\chi_1 + \chi_2)A - \frac{V_T}{2} = C + De^{zb} + V_T F, \quad (\chi_3 + \chi_4)B + \frac{V_T}{2} = Ce^{zb} + D + V_T F, \quad (\text{S40})$$

and the boundary layer ODEs (S29)-(S30) give

$$i\omega A = \frac{qD_P N_0 z}{V_T} (C - De^{zb}), \quad i\omega B = -\frac{qD_P N_0 z}{V_T} (Ce^{zb} - D). \quad (\text{S41})$$

We therefore have four constraints on $A, B, C,$ and D :

$$\begin{pmatrix} \chi_1 + \chi_2 & 0 & -1 & -e^{zb} \\ 0 & \chi_3 + \chi_4 & -e^{zb} & -1 \\ \frac{i\omega V_T}{qD_P N_0} & 0 & -z & ze^{zb} \\ 0 & \frac{i\omega V_T}{qD_P N_0} & ze^{zb} & -z \end{pmatrix} \begin{pmatrix} A \\ B \\ C \\ D \end{pmatrix} = V_T \begin{pmatrix} F + \frac{1}{2} \\ F - \frac{1}{2} \\ 0 \\ 0 \end{pmatrix} \quad (\text{S42})$$

with solutions

$$A = \frac{zqD_P N_0}{i\omega} \frac{2(F - 1/2)e^{zb} + (F + 1/2)(X_R - 1 - (X_R + 1)e^{2zb})}{(X_L - 1)(X_R - 1) - (X_R + 1)(X_L + 1)e^{2zb}} \quad (\text{S43})$$

$$B = \frac{zqD_P N_0}{i\omega} \frac{2(F + 1/2)e^{zb} + (F - 1/2)(X_L - 1 - (X_L + 1)e^{2zb})}{(X_L - 1)(X_R - 1) - (X_R + 1)(X_L + 1)e^{2zb}} \quad (\text{S44})$$

$$C = V_T \frac{(F + 1/2)(X_R - 1) + (F - 1/2)(X_L + 1)e^{zb}}{(X_L - 1)(X_R - 1) - (X_R + 1)(X_L + 1)e^{2zb}} \quad (\text{S45})$$

$$D = V_T \frac{(F - 1/2)(X_L - 1) + (F + 1/2)(X_R + 1)e^{zb}}{(X_L - 1)(X_R - 1) - (X_R + 1)(X_L + 1)e^{2zb}} \quad (\text{S46})$$

where

$$X_L = \frac{(\chi_1 + \chi_2)zqD_P N_0}{i\omega V_T}, \quad X_R = \frac{(\chi_3 + \chi_4)zqD_P N_0}{i\omega V_T}. \quad (\text{S47})$$

We have thus obtained analytic approximate solutions for $\phi(x, t), Q_L(t),$ and $Q_R(t).$

1.6 The DC current problem

Calculation of the current density through the device requires solution of (S19)-(S21) on the background electric potential solution. While in the DC steady state, the carrier densities are determined by ϕ^{DC} :

$$n^{\text{DC}} = d_E k_E e^{-\frac{v_1^{\text{DC}} - v_2^{\text{DC}}}{V_T}}, \quad p^{\text{DC}} = d_H k_H e^{-\frac{-v_3^{\text{DC}} - v_4^{\text{DC}}}{V_T}}. \quad (\text{S48})$$

The DC bulk and surface recombination rates can be chosen are, to good approximation,

$$R^{\text{DC}} = \begin{cases} \frac{n^{\text{DC}}}{t_n} & \text{if electron-limited} \\ \frac{p^{\text{DC}}}{t_p} & \text{if hole-limited} \end{cases} \quad (\text{S49})$$

$$R_l^{\text{DC}} = \nu_p^E e^{-V_2^{\text{DC}}/V_T} p^{\text{DC}}, \quad (\text{S50})$$

$$R_r^{\text{DC}} = \nu_n^H e^{-V_3^{\text{DC}}/V_T} n^{\text{DC}}. \quad (\text{S51})$$

The current density ODEs (S19)-(S20) can then be integrated to obtain

$$j^{n\text{DC}}(x) = q \left[\int_x^b G(x) dx - (b-x)R^{\text{DC}} - R_r^{\text{DC}} \right], \quad j^{p\text{DC}}(x) = q \left[\int_0^x G(x) dx - xR^{\text{DC}} - R_l^{\text{DC}} \right], \quad (\text{S52})$$

and a total DC current density ($J = j^n + j^p$) of

$$J^{\text{DC}} = q \left[\int_0^b G(x) dx - bR^{\text{DC}} - R_l^{\text{DC}} - R_r^{\text{DC}} \right]. \quad (\text{S53})$$

1.7 Linearising the current problem

It remains to determine the AC component of the current density. The recombination rates are linearised (in terms of the perturbation amplitude δ) as

$$R = R^{\text{DC}} + \delta R^{\text{AC}}, \quad R_l = R_l^{\text{DC}} + \delta R_l^{\text{AC}}, \quad R_r = R_r^{\text{DC}} + \delta R_r^{\text{AC}}, \quad (\text{S54})$$

and carrier densities as

$$n = n^{\text{DC}} + \delta n^{\text{AC}}, \quad p = p^{\text{DC}} + \delta p^{\text{AC}}. \quad (\text{S55})$$

The AC recombination rates can be calculated as

$$R^{\text{AC}} = \begin{cases} \frac{n^{\text{AC}}}{\tau_n} & \text{if electron-limited } (\tau_p \ll \tau_n) \\ \frac{p^{\text{AC}}}{\tau_p} & \text{if hole limited } (\tau_p \gg \tau_n) \end{cases} \quad (\text{S56})$$

$$R_l^{\text{AC}} = \nu_p^E e^{-V_2^{\text{DC}}/V_T} \left(p^{\text{AC}}|_{x=0} - \frac{p^{\text{DC}}}{V_T} V_2^{\text{AC}} \right), \quad (\text{S57})$$

$$R_r^{\text{AC}} = \nu_n^H e^{-V_3^{\text{DC}}/V_T} \left(n^{\text{AC}}|_{x=b} - \frac{n^{\text{DC}}}{V_T} V_3^{\text{AC}} \right), \quad (\text{S58})$$

and the AC current densities are functions of ϕ^{AC} (see Eq. S21):

$$n^{\text{AC}} = n^{\text{DC}} \left(\frac{\phi^{\text{AC}}}{V_T} + \frac{1}{2} e^{i\omega t} \right), \quad p^{\text{AC}} = p^{\text{DC}} \left(\frac{-\phi^{\text{AC}}}{V_T} + \frac{1}{2} e^{i\omega t} \right). \quad (\text{S59})$$

The current density ODEs (S19)-(S20) are linearised (in δ) and integrated to obtain electron and hole current densities

$$j^{n\text{AC}} = -q \int_x^b R^{\text{AC}} dx - qR_r^{\text{AC}}, \quad j^{p\text{AC}} = -q \int_0^x R^{\text{AC}} dx - qR_l^{\text{AC}}, \quad (\text{S60})$$

with a total current density

$$J^{\text{AC}} = -q \left[\int_0^b R^{\text{AC}} dx + R_l^{\text{AC}} + R_r^{\text{AC}} \right] - \varepsilon_p \frac{\partial}{\partial t} \frac{\partial \phi^{\text{AC}}}{\partial x} \quad (\text{S61})$$

where the last term arises from the displacement current density. The total current density is parameterised as

$$J^{\text{AC}} = (\mathcal{J}_R + \mathcal{J}_d) e^{i\omega t} \quad (\text{S62})$$

where \mathcal{J}_R results from the recombination current and can take one of four forms to isolate a single recombination pathway that dominates at the DC voltage:

$$\mathcal{J}_R = \begin{cases} -\frac{qn^{\text{DC}}}{\tau_n} \left[b \left(\frac{1}{2} + F \right) + \frac{C+D}{zV_T} (e^{zb} - 1) \right] & \text{electron-limited bulk SRH} \\ -\frac{qp^{\text{DC}}}{\tau_p} \left[b \left(\frac{1}{2} - F \right) - \frac{C+D}{zV_T} (e^{zb} - 1) \right] & \text{hole-limited bulk SRH} \\ -\frac{qp^{\text{DC}} \nu_p^E}{V_T} e^{-\frac{V_2^{\text{DC}}}{V_T}} \left[\left(\frac{1}{2} - F \right) V_T - C - D e^{zb} + \chi_2 A \right] & \text{ETL-PAL surface SRH} \\ -\frac{qn^{\text{DC}} \nu_n^H}{V_T} e^{-\frac{V_3^{\text{DC}}}{V_T}} \left[\left(\frac{1}{2} + F \right) V_T + C e^{zb} + D - \chi_3 B \right] & \text{HTL-PAL surface SRH} \end{cases} \quad (\text{S63})$$

and

$$\mathcal{J}_d = -\varepsilon_p i \omega z \left(C e^{zx} - D e^{z(b-x)} \right) \quad (\text{S64})$$

arises from the displacement current. Note that the displacement current here is x -dependent but comparison with numerical solutions shows that it should be sampled at $x = 0$ if $n^{\text{DC}} < p^{\text{DC}}$ and $x = b$ otherwise. The total impedance measured can be calculated as

$$Z(\omega) = \frac{-V_T}{\mathcal{J}_R + \mathcal{J}_d}. \quad (\text{S65})$$

Note that we adopt a negative sign to account for our definition of voltage such that an increase in voltage results in a decrease in current density.

1.8 Capacitance

The capacitance of the device is defined as

$$\mathcal{C} = \frac{1}{\omega} \text{Im} \left(\frac{1}{Z} \right). \quad (\text{S66})$$

The general capacitance, as a function of (angular) frequency, in the mSPM is therefore

$$\mathcal{C}(\omega) = \frac{-1}{\omega} \text{Im} \left(\frac{\mathcal{J}_R + \mathcal{J}_d}{V_T} \right). \quad (\text{S67})$$

In the high-frequency limit ($\omega \rightarrow \infty$) the displacement current dominates this expression. The high frequency limit of capacitance can therefore be calculated as

$$\mathcal{C}_{\text{HF}} = \frac{\varepsilon_p}{b} \frac{\hat{z} (e^{2\hat{z}} + 1)}{e^{2\hat{z}} - 1} \quad (\text{S68})$$

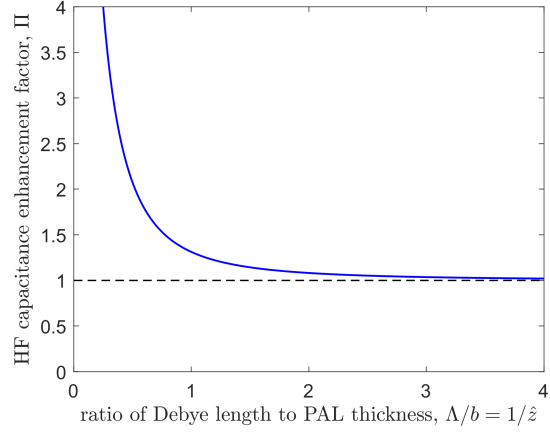


Figure S3: Enhancement of the high frequency capacitance beyond the geometric capacitance ($\Pi = 1$) as carrier Debye length (Λ) becomes small relative to the PAL width (b).

where $\hat{\zeta} = b/\Lambda$ is the ratio of the perovskite layer thickness and the dominant carrier Debye length. This corresponds to an enhancement of the high-frequency capacitance relative to the geometric capacitance by some factor

$$\Pi(\hat{\zeta}) = \frac{\hat{\zeta} (e^{2\hat{\zeta}} + 1)}{e^{2\hat{\zeta}} - 1}. \quad (\text{S69})$$

This factor is plotted against carrier Debye length in Figure S3. If both carrier densities are small, such that both Debye lengths are much greater than the PAL thickness, the geometric capacitance, $\mathcal{C}_{\text{HF}} = \varepsilon/b$ is recovered.

| Quantity | Symbol | Cell A | Cell B | Cell C | Cell D | Cell E | Cell F | Cell G1 | Cell G2 |
|---|--------------|----------------------|----------------------|----------------------|----------------------|----------------------|----------------------|----------------------|----------------------|
| Perovskite layer | | | | | | | | | |
| thickness [nm] | b | 300 | 400 | 300 | 400 | 400 | 400 | 400 | 400 |
| relative permittivity | ϵ_p | 16 | 24.1 | 24.1 | 24.1 | 24.1 | 24.1 | 24.1 | 24.1 |
| absorption coefficient [m^{-1}] | α | 1.3×10^7 | 1.3×10^7 | 1.3×10^7 | 1.3×10^7 | 1.3×10^7 | 1.3×10^7 | 1.3×10^7 | 1.3×10^7 |
| conduction band minimum [eV] | E_c^c | -3.8 | -3.75 | -3.8 | -3.75 | -3.8 | -3.9 | -3.75 | -3.75 |
| valence band maximum [eV] | E_v^c | -5.4 | -5.45 | -5.3 | -5.3 | -5.4 | -5.6 | -5.5 | -5.4 |
| electron diffusion coefficient [$\text{cm}^2 \text{s}^{-1}$] | D_n^c | 1.7 | 17 | 1.7 | 1.7 | 1.7 | 1.7 | 1.7 | 1.7 |
| hole diffusion coefficient [$\text{cm}^2 \text{s}^{-1}$] | D_p^c | 17 | 17 | 1.7 | 1.7 | 0.017 | 1.7 | 1.7 | 1.7 |
| conduction band effective DoS [m^{-3}] | g_c^c | 8.1×10^{24} | 8.1×10^{24} | 8.1×10^{24} | 8.1×10^{24} | 8.1×10^{24} | 8.1×10^{24} | 8.1×10^{24} | 8.1×10^{24} |
| valence band effective DoS [m^{-3}] | g_v^c | 5.8×10^{24} | 5.8×10^{24} | 5.8×10^{24} | 5.8×10^{24} | 5.8×10^{24} | 5.8×10^{24} | 5.8×10^{24} | 5.8×10^{24} |
| average density of ion vacancies [m^{-3}] | N_0 | 1.6×10^{25} | 1.6×10^{25} | 1.6×10^{25} | 5×10^{24} | 5×10^{24} | 1.6×10^{25} | 5×10^{24} | 5×10^{24} |
| ion vacancy diffusion coefficient [$\text{cm}^2 \text{s}^{-1}$] | D_P | 3×10^{-14} | 10^{-12} | 5×10^{-12} | 10^{-12} | 10^{-12} | 10^{-12} | 2×10^{-11} | 4×10^{-12} |
| Electron transport layer | | | | | | | | | |
| thickness [nm] | b | 100 | 100 | 100 | 100 | 100 | 100 | 100 | 100 |
| relative permittivity | ϵ_E | 10 | 20 | 3 | 10 | 15 | 10 | 15 | 12 |
| conduction band minimum [eV] | E_c^E | -4.1 | -4.1 | -4.1 | -4.1 | -3.96 | -4.1 | -4.1 | -4.1 |
| electron diffusion coefficient [$\text{cm}^2 \text{s}^{-1}$] | D_E^E | 0.1 | 0.1 | 0.1 | 0.1 | 1 | 0.1 | 0.1 | 0.1 |
| conduction band effective DoS [m^{-3}] | g_c^E | 10^{26} | 10^{26} | 10^{26} | 10^{26} | 10^{26} | 10^{26} | 10^{26} | 10^{26} |
| effective doping density [m^{-3}] | d_E^E | 5×10^{24} | 5×10^{24} | 5×10^{24} | 5×10^{24} | 5×10^{24} | 5×10^{24} | 5×10^{24} | 5×10^{24} |
| Hole transport layer | | | | | | | | | |
| thickness [nm] | b_H | 200 | 200 | 200 | 200 | 200 | 200 | 200 | 200 |
| relative permittivity | ϵ_H | 2 | 2 | 10 | 3 | 1.5 | 3 | 2 | 3 |
| valence band maximum [eV] | E_v^H | -5.1 | -5.1 | -5.1 | -5.12 | -5.1 | -5.3 | -5.22 | -5.24 |
| hole diffusion coefficient [$\text{cm}^2 \text{s}^{-1}$] | D_H^H | 0.01 | 0.01 | 0.01 | 0.01 | 0.1 | 0.01 | 0.01 | 0.01 |
| valence band effective DoS [m^{-3}] | g_v^H | 10^{26} | 10^{26} | 10^{26} | 10^{26} | 10^{26} | 10^{26} | 10^{26} | 10^{26} |
| effective doping density [m^{-3}] | d_H^H | 1×10^{24} | 5×10^{23} | 3×10^{24} | 5×10^{24} | 5×10^{23} | 5×10^{24} | 2×10^{24} | 5×10^{24} |
| Recombination parameters | | | | | | | | | |
| SRH electron pseudo-lifetime [s] | τ_n | 7.5×10^{-9} | 10^{-10} | 10^{-6} | 10^{-10} | 5×10^{-6} | 10^{-9} | 10^{-9} | 10^{-10} |
| SRH hole pseudo-lifetime [s] | τ_p | 10^{-11} | 10^{-7} | 10^{-9} | 5×10^{-6} | 10^{-10} | 10^{-6} | 8×10^{-8} | 5×10^{-6} |
| bimolecular recombination rate [$\text{m}^3 \text{s}^{-1}$] | β | 0 | 0 | 0 | 0 | 0 | 0 | 0 | 0 |

Table S1: Parameter sets used in numerical drift-diffusion simulations performed using IonMonger [60, 61].

2 Simulated capacitance plots

As discussed in the main text, the capacitance plots corresponding to each of the simulated Nyquist plots are included here for completeness.

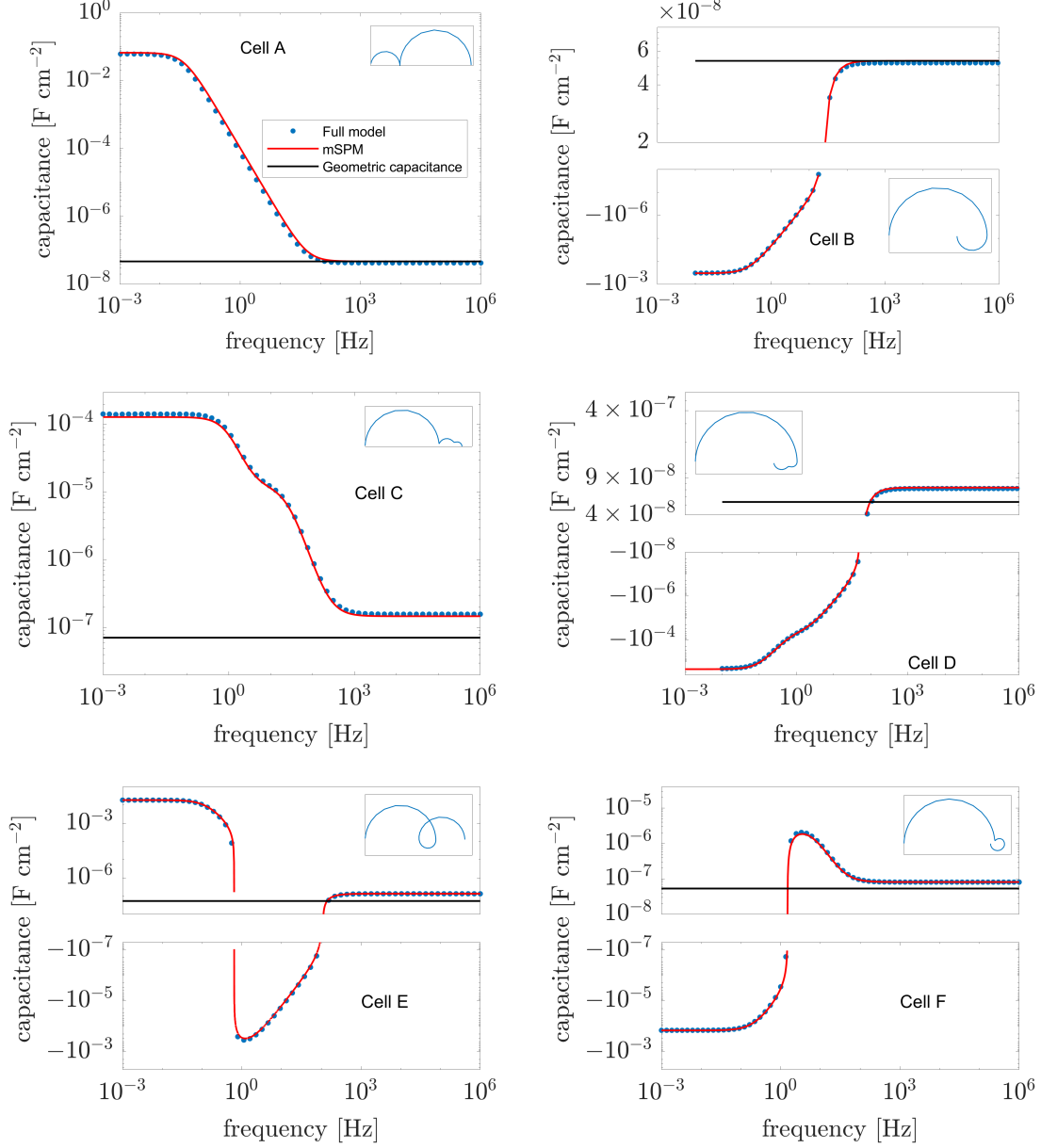


Figure S4: Capacitance plots from simulated impedance spectra of Cells A-F as shown in Figures 7,8,11-14. Blue circles are obtained from simulation of the full DD model in IonMonger and red lines the mSPM. Black lines show the theoretical geometric capacitance of the perovskite layer. Nyquist plots are shown in the insets.

3 Spectra simulated with bi-molecular recombination

As discussed in the main text, simulated Nyquist plots including bi-molecular recombination (with rate constant $10^{-10} \text{ cm}^3\text{s}^{-1}$) are included here for completeness.

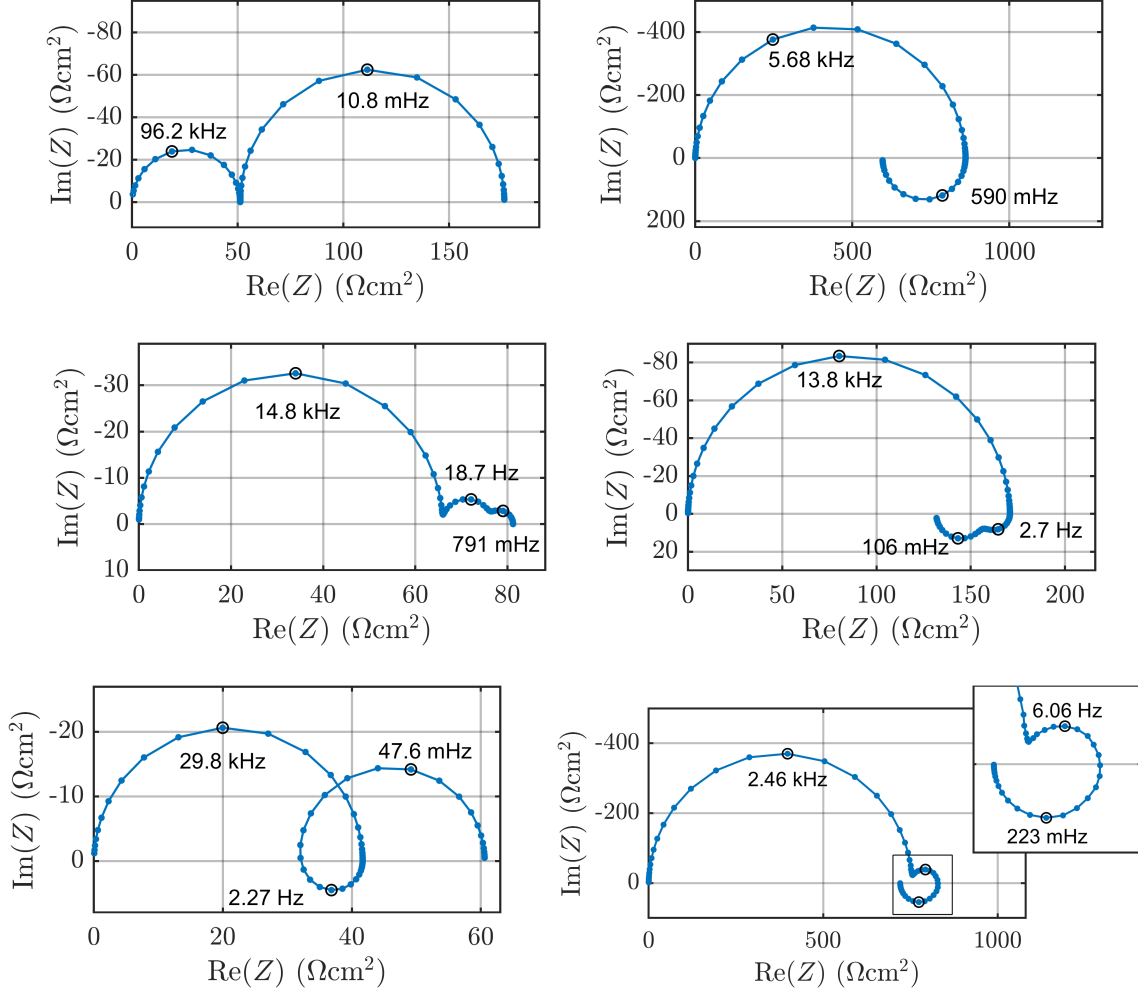


Figure S5: Simulated Nyquist plots from Cells A-F as shown in Figures 7,8,11-14 with the addition of bi-molecular recombination.

4 Particle densities in each frequency regime

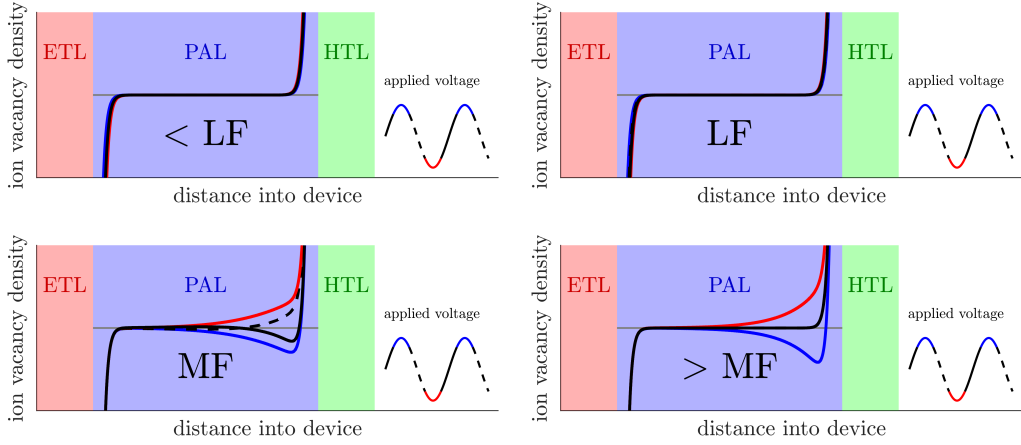


Figure S6: Ion vacancy density in each frequency regime. Impedance features occur when the black dashed line does not coincide with the black solid line, *i.e.* the system has a phase delay. Note that oscillations are greatly exaggerated in these illustrative plots. In this example, the ETL-perovskite band offset is small.

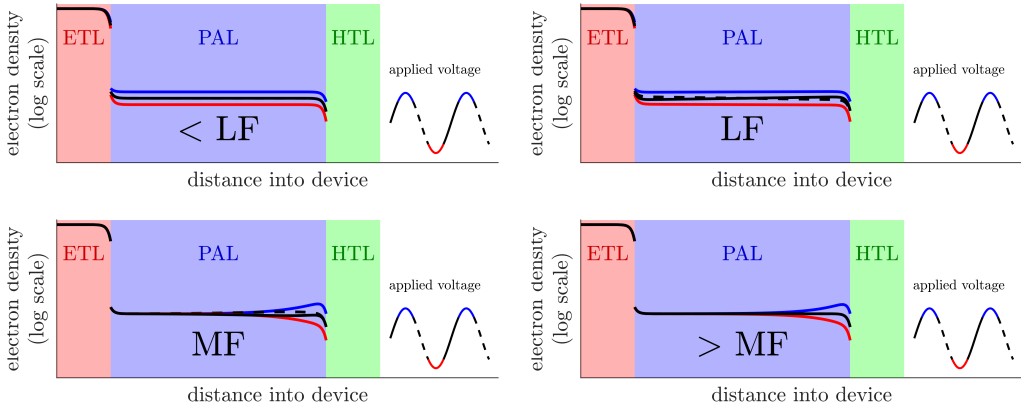


Figure S7: Electron density in each frequency regime. Impedance features occur when the black dashed line does not coincide with the black solid line, *i.e.* the system has a phase delay. Note that oscillations are greatly exaggerated in these illustrative plots. In this example, the ETL-perovskite band offset is small.

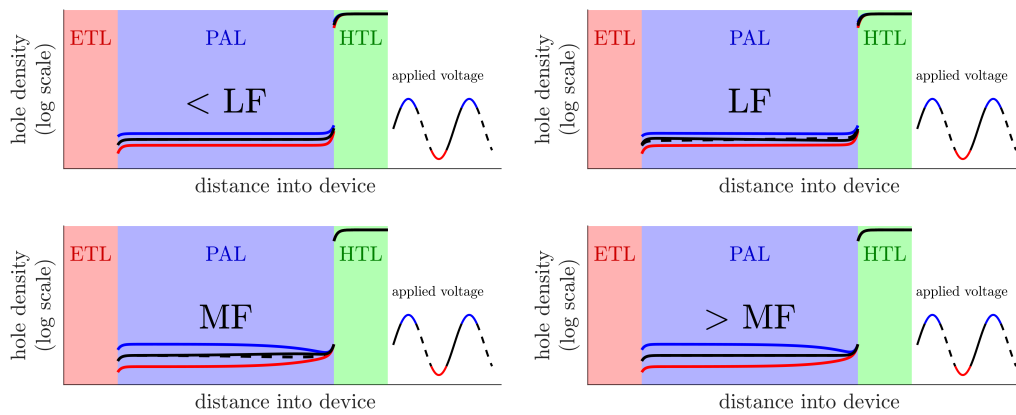


Figure S8: Hole density in each frequency regime. Impedance features occur when the black dashed line does not coincide with the black solid line, *i.e.* the system has a phase delay. Note that oscillations are greatly exaggerated in these illustrative plots. In this example, the ETL-perovskite band offset is small.